Optomechanical imaging system for breast cancer detection

Rabah Al abdi,[1] Harry L. Graber,[1,2] Yong Xu,[1,2] and Randall L. Barbour[1,2,*]

[1]*Department of Pathology, SUNY Downstate Medical Center, Box 25, 450 Clarkson Avenue, Brooklyn, New York 11203, USA*
[2]*NIRx Medical Technologies, LLC, Glen Head, New York 11545, USA*
**Corresponding author: randall.barbour@downstate.edu*

Received April 8, 2011; revised September 2, 2011; accepted September 6, 2011; posted September 26, 2011 (Doc. ID 145596); published November 11, 2011

Imaging studies of the breast comprise three principal sensing domains: structural, mechanical, and functional. Combinations of these domains can yield either additive or wholly new information, depending on whether one domain interacts with the other. In this report, we describe a new approach to breast imaging based on the interaction between controlled applied mechanical force and tissue hemodynamics. Presented is a description of the system design, performance characteristics, and representative clinical findings for a second-generation dynamic near-infrared optical tomographic breast imager that examines both breasts simultaneously, under conditions of rest and controlled mechanical provocation. The expected capabilities and limitations of the developed system are described in relation to the various sensing domains for breast imaging.

OCIS codes: 120.5475, 100.6950, 170.1610, 170.3830, 170.4580, 170.2655.

1. INTRODUCTION

Breast cancer remains the leading cause of newly diagnosed cases of cancer among women in the United States and the second leading cause of cancer deaths [1]. Currently, breast cancer screening is achieved using either structural imaging methods (e.g., x-ray mammography) or by tactile sensing as part of the clinical breast exam (CBE). For the latter, the principal considerations are architectural and surface distortions in breast shape, evidence of bilateral asymmetry, and local differences in tissue stiffness. Also available are diagnostic imaging technologies that exploit different aspects of the tumor phenotype. For instance, gadolinium-enhanced magnetic resonance imaging (MRI) [2] exploits increased leakiness commonly associated with the tumor microvasculature [2–4].

By introducing low-amplitude mechanical vibrations to the breast, magnetic resonance (MR) elastography [5,6] can detect the increased tissue stiffness also commonly associated with cancerous tumors. Similarly, ultrasound (US) imaging can be used for diagnostic studies of the breast [7], or, when US is combined with mechanical sources, US elastography can measure local variations in tissue stiffness [8,9]. Among the functional imaging technologies, various types of positron emitting isotopes can be used to explore metabolic transformations [10,11] or the presence of trace levels of tissue constituents [12].

Increasingly, promising approaches for exploiting key elements of the tumor phenotype involve near-infrared (NIR) optical methods. When configured to support multisensor arrays, tomographic images of the absorption and scattering properties of the tissue can be obtained [13,14]. Measurements of this type typically have been employed along two distinct lines. In one case, the goal is to achieve absolute measures of key constituents of the tissue that interact with the penetrating light. Among the features that have been described using this approach are elements of the hemoglobin (Hb) signal, tissue water, lipid, and measures of scattering amplitude and scattering power [15]. The other approach is to define dynamic responses of the tissue based on measures of relative changes in the optical signal [16,17]. While not easily supporting absolute constituent measures, this approach has the added benefit of exploring any of a host of dynamic features associated with Hb signals that may occur spontaneously (e.g., vascular rhythms) [18] or can be induced by controlled provocations [19,20]. In a previous report, we described a system that can dynamically image both breasts simultaneously and provided evidence of enhanced tumor detection from a simple respiratory maneuver [21]. Although promising, the need for subject compliance makes practical use of this approach challenging.

Regardless of the potential success that ultimately might be achieved from measures of optical-signal dynamics, the fact remains that the information quality is unavoidably degraded by the low spatial resolution inherent to the diffuse optical method. One approach to improve on this has been to combine optical studies with additional imaging technologies that are capable of producing high-resolution images of the breast. Systems combining NIR with x-ray [22], US [23], or MR [24] imaging have been developed in support of this goal. While such combinations are useful, because the sensing domains that they comprise do not physically interact, the information derived is additive. By contrast, interaction of sensing domains offers the potential for deriving wholly new contrast features. A good example of this is the already mentioned elastography techniques.

In this report, we introduce the method of optomechanical imaging as a basis for obtaining new contrast features in the hope of improving the diagnostic potential of NIR imaging methods for breast cancer detection. Central to this technique is the ability to simultaneously measure the viscoelastic properties of the breast while observing time-dependent changes

in hemodynamics induced through precisely controlled articulation. Because deformation of the breast produces a time-varying viscoelastic response, whose details will depend on the specifics of the applied force (e.g., amplitude, rate, duration, articulation dynamics), which in turn will affect breast hemodynamics, it is evident that the process of measuring the viscoelastic stress–strain response is *inherently interactive* with concurrent optical measures. This is a significant consideration, as it affords the possibility of deriving a wide range of *force-dependent* contrast features, especially with regard to the hemodynamic response, which itself can be additionally modified by factors that are known to influence hemodynamics (e.g., respiratory gases, pharmacological agents). Thus, we anticipate the potential to harness a wide range of new contrast features whose details are linked to the constitutive viscoelastic and hemodynamic states of the breast, both of which are strongly affected by tumorigenesis.

The spirit of this technique has been motivated by a growing number of reports that have sought to implement applied-force techniques in combination with NIR studies of the breast [25–30]. However, notably different here are three new capabilities: (i) extension of the applied-force maneuvers to include measures of strain, (ii) introduction of feedback-controlled sensing of the articulating members, thereby allowing for controlled measures of stress relaxation and creep [31,32], and (iii) the capability of high-precision articulation under a wide range of conditions.

2. SYSTEM DESCRIPTION

The system developed is an extension of a previously described simultaneous bilateral breast imaging system [21]. Data collection is based on performing a time-multiplexed continuous-wave (CW) optical measurement with parallel data capture and automated gain adjustment. A schematic and photograph of the imager is shown in Fig. 1. Principal elements include laser sources and coupling optics (1), two-stage optical switch (2), optical fibers (3), sensor heads and support arms (4), stepper motor driver (5), detector modules (6), servo-motor controller (7), host computer (8), and system power supply (9).

Novel elements of the new system include high-density optical sensing heads (8192 channels) having fast, feedback-controlled, force-sensing, articulating members that can conform to a wide range of breast sizes, and the ability to perform optomechanical scans with the subject in the seated position. A user interface has been developed to support two different modes of sensing-head control: time-dependent stress relaxation under fixed deformation, and time-dependent deformation under fixed applied force (creep). In both modes, optical measurements from all sensing channels are continuously recorded. In all, the developed system provides three sets of measurements: optical, applied force, and deformation.

Detailed descriptions of the major submodules and their design objectives are presented in the following subsections.

A. Closed-Loop Controlled, Articulating Sensing Head

Key goals in the design of the articulating assembly were the ability to accommodate a wide range of breast sizes and to enable simultaneous bilateral measurements of the viscoelastic and hemodynamic responses to articulation. An additional design goal was to impose articulation on a time scale sufficiently fast (<2 s) as to offer the opportunity of observing the initial hemodynamic response, associated with the high compliance of the venous circulation, to applied force [27]. For simplicity, design constraints were limited to use of addressable motor drives rather than use of hydraulic manifolds, smart materials, or other strategies. It was also recognized that the presence of fibers attached to the articulating units could introduce drag during movements, rendering measures of applied force inaccurate or unstable. Still another consideration was the understanding that intersubject variability in the natural contour of the breast [33] called for adoption of a conforming interface.

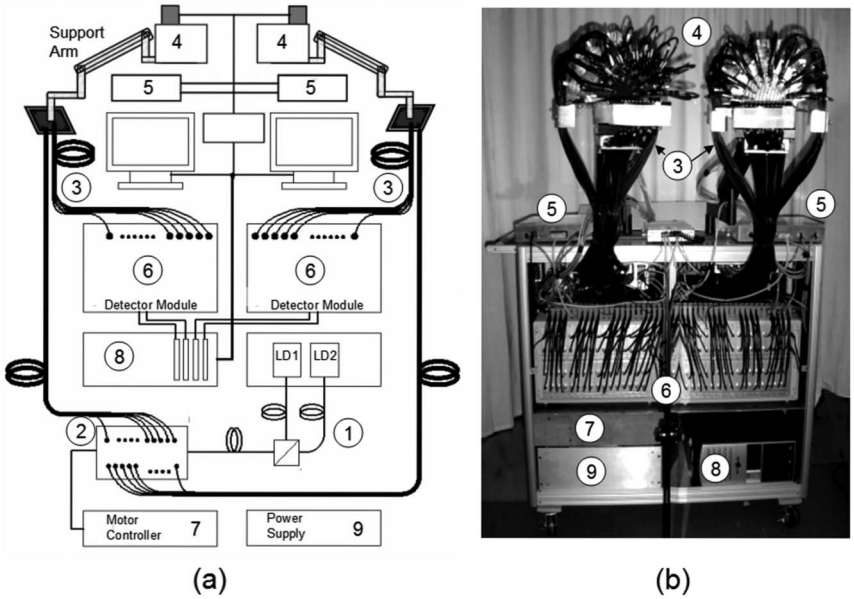

Fig. 1. Developed dual-breast articulating imager. (a) Schematic and (b) photograph of imager: laser sources and coupling optics (1), two-stage optical switch (2), illumination and detection fiber optics (3), sensor heads and support arms (4), stepper motor drivers (5), detector modules (6), servo-motor controller (7), host computer (8), and system power supply (9). LD, laser diode.

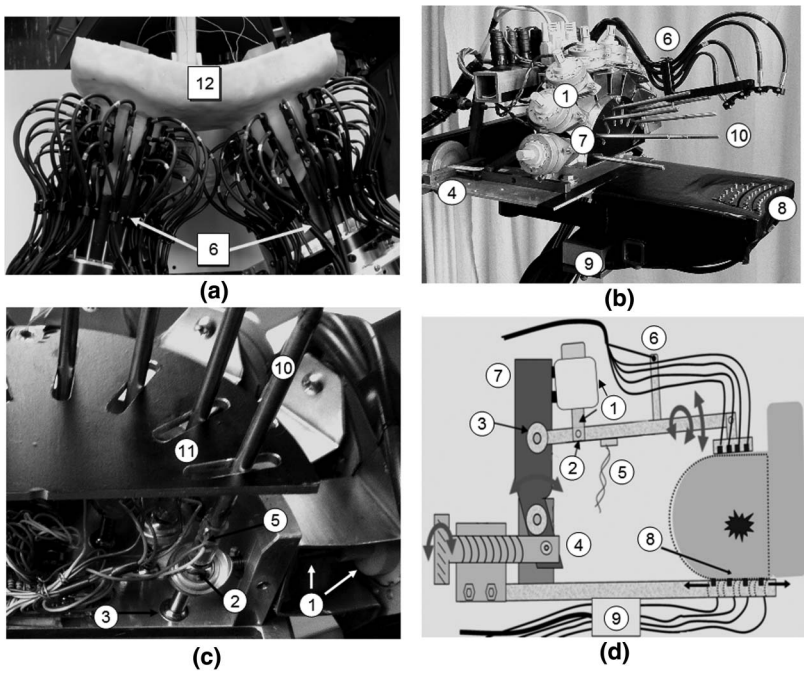

Fig. 2. Articulating sensing head. (a) Photograph of the dual-breast sensing head positioned onto a torso phantom; (b) photograph of exposed individual articulating unit; (c) photograph of internal coupling mechanics; (d) functional schematic of the principal design features.

Shown in Fig. 2 is a photograph of the fully assembled articulating sensing head positioned onto a fabricated partial female torso [Fig. 2(a)], along with photographs that highlight an individual articulating unit [Fig. 2(b)] and its internal coupling mechanics [Fig. 2(c)], and a functional schematic of the principal design features [Fig. 2(d)]. Principal elements of the head include stepper motor and drive shaft (1), coupling mechanics (2, 3), sensor housing coupling joint (4), strain gauge (5), fiber-support element (6), upper sensor assembly (7), lower sensor assembly (8), fiber strain relief (9), lever rod (10), and guide channel (11). Each sensing head houses 64 light-receiving optodes, half of which also serve for light delivery in a colocated configuration: these are equally divided between the top and bottom arrays and are arranged in an alternating pattern. In all, each measuring head performs 2048 multidistance optical measurements per wavelength per image frame and operates at approximately a 2 Hz framing rate.

1. Functional Properties of Sensor Head Design

Active Drive Mechanics of Articulating Sensor Array

Two distinct strategies for effecting movement of the articulating units are drive-coupling mechanisms that are either mechanically leveraged or not. An advantage offered by leveraging is that it can be used to either enhance torque at the expense of speed or vice versa. Also, because of the myriad of design approaches inherent to leveraging schemes, in many instances these are most adaptive for meeting specific requirements.

The leveraging scheme adopted here produced approximately an 8∶1 advantage in speed of movement of the articulating unit, with a corresponding decrease in torque at the point of contact with the breast. The maximum amplitude of the latter was of the order of 8 N. Particulars of leveraging, illustrated in Figs. 2(c) and 2(d), include a two-point mechanism and lever, wherein one point is attached to the motor shaft using a rod-end bearing that features a center hole and surrounding swivel bearing (2), while the other point is a ball joint attached to the end of the lever rod and anchored into the support housing (3). The former was adopted in order to accommodate the vertical slippage of the swivel housing relative to the lever rod that occurs upon linear movement of the motor shaft. With this design, linear movement of the motor shaft produces an arclike movement of the lever rod. However, because of the added degrees of freedom inherent to a ball joint, its use can introduce unwanted angular drift. This was limited by introduction of a restrictive guide channel [11 in Fig. 2(c)] that has a projected orientation to a central point. With this orientation, coordinated movement of the complete array maximally favors a focus of reactive force within the most central regions of the breast.

Motorized movement of the lever arm was achieved using a linear stepper motor (part number 42DBL10C2B-K, Danaher Motion Co.). The selected motors were chosen because they offer sufficient speed, are powerful for their size, and have excellent resolution of movement (0.0254 mm per pulse). A position encoder is not necessary as counting the number of pulses sent to the motor determines the position of the motor shaft.

Articulating Unit

Design objectives included the need to provide rigid support for the attached optodes, drag-free movement upon articulation, and contouring to the breast surface. A two-component device was developed, consisting of the lever arm and fiber-support element (items 10 and 6 in Fig. 2, respectively). The latter is a sleeved attachment that fits firmly over the lever rod shaft and includes three design features. Located at the lower aspect of the sleeve is a fiber organizer that also serves as a strain relief. Located in the middle is a cutout along the longitudinal axis to provide for passage of fibers from the organizer to a terminal element, located at the top, that has an

arclike shape and pivots to allow for contouring to the breast surface.

Simply introducing fibers within the sleeved attachment does not, by itself, eliminate resistance to movement due to drag. To minimize this, it was necessary to offset the fibers from the surrounding motor assemblies and to introduce sufficient slack between the fiber organizer and terminal support arc in a stepped fashion [see Fig. 2(b)]. The latter has the effect of causing the arc to assume a neutral position while retaining good pivoting capability, thereby conforming to the natural contour of the breast upon light contact.

Verification that the overall design features of the sensor head accomplished our goals was experimentally established by driving the articulating units over the full range of motion (90 mm), in both directions, while recording changes in stress as a measure of drag. Results obtained showed that the maximum stress amplitude was of the order of <10% of the minimum contact force applied to the breast (1.8 N) and <3% of the maximum force.

Lower Sensor Array Design

Key design objectives included the ability to explore different breast sizes in a manner consistent with their roughly parabolic shape in the supported orientation and the capacity to perform measures that include regions immediately adjacent to the chest wall. Adopted was an array comprising four nested arcs [item 8, Figs. 2(b) and 2(d)] of different lengths that varied such that a roughly parabolic contour was retained, irrespective of the fixed distance separating each arc. In this fashion, the array size can be adjusted, if required, to different breast sizes without changing its overall basic shape.

Mechanical Assemblies to Accommodate Positioning of Breast within the Sensor Head

While the above designs provide for motor-driven articulation with attached fibers, additional design features are required to facilitate positioning of the breast within the sensor head with the subject in the seated position. Three principal design features were implemented.

First was the use of high-load support arms that can support the sensor assembly in a cantilevered position [Fig. 1(a)]. To ensure stability and ease of positioning of an otherwise high-load design, the entire assembly is rendered neutrally buoyant by an internal spring-loaded mechanism housed within the armature. Once final positioning is established, the armature is stabilized with locking mechanisms.

The second design feature addresses the need for mechanical assemblies that support the introduction of the breast within the sensor head once its final position against the chest wall has been established. The simplest solution was to introduce a pivot assembly [item 4, Figs. 2(b) and 2(d)], mechanically linked to the bottom array, that serves to open and close the top sensor array. In practice, following manual adjustment of the top array to within a few millimeters of the breast surface, feedback-controlled contact with the breast at a desired force was accomplished using commands available through the developed sensor control graphical user interface (GUI) (see the "Articulation Control and Calibration: 4. Controlling Software" subsection below).

Finally, while the above designs achieve articulation and accommodate the various modes of adjustment necessary for appropriate final positioning of the sensor heads, such flexibility can introduce backlash within the adjustable assemblies thereby degrading the accuracy of measures of applied force and tissue deformation measures. Backlash was eliminated by introducing a locking mechanism that secures the orientation of the top assembly housing once final positioning has been achieved and by ensuring that the force applied to the breast does not fall below a minimum needed to overcome backlash within the motor assembly (≥0.4 N).

Articulation Control and Calibration

The closed-loop control mechanism comprises three principal elements: (1) strain gauges affixed to the articulation elements, (2) motor driver that provides power and digital lines for control of the stepper motors, and (3) software for display, data storage, acquisition of sensor response, and control of articulation.

2. Strain Gauges

Applied force was measured by a semiconductor strain gauge affixed to a milled flat located near the base of the articulating elements (Micron Instruments, Inc., California, Model SS-090-060-500P-S1). Bonding (M-Bond 610 adhesive), and heat treatment (16 h at 150°C) was performed in accordance with the manufacturer's specifications. Force-dependent changes in resistance are converted to voltage using a voltage divider and are subsequently sampled using a data acquisition card (National Instruments, Model USB-6229). Calibration curves, corrected for ambient temperature, are linear (~5.7 Ω/N) with <1% deviation over a range of 15 N.

3. Motor Driver

Two integrated circuits (STMicroelectronics, Models L297 and L298), arranged in series, are used to provide the required four-phase drive signals and power conditioning needed for motor control. Direction, on–off status, and driving speed of the motors are specified through a LabView interface that translates commands to transistor–transistor logic pulses through the USB-6229 card. The frequency of these pulses and the sequence of the driving signals control the motor speed and direction, respectively. To reduce noise, shielded cables are used to provide connections between the USB card, motor driver, and motors.

4. Controlling Software

Figure 3 shows a screen shot of the GUI used to control and display results of the measured positions and applied forces of the articulating units. Two modes of operation are supported: motor movements to maintain a constant applied force (creep studies) and movements to achieve an initial target force under fixed deformation (stress-relaxation studies). In the former case, input values are reached to within a user-defined tolerance limit, while the distance that the articulating units must travel to maintain the target force is unrestrained. In the latter case, the user input is the initial target force {up to 8 N [1800 millipounds (mlb)] of force}, and the distance traveled needed to achieve this is unrestrained.

The windows in the top half of the GUI display traces of the force applied to the left and right breasts for each articulating unit (1). In the middle are controls for uploading of files for automated control of a specified protocol (2), real-time

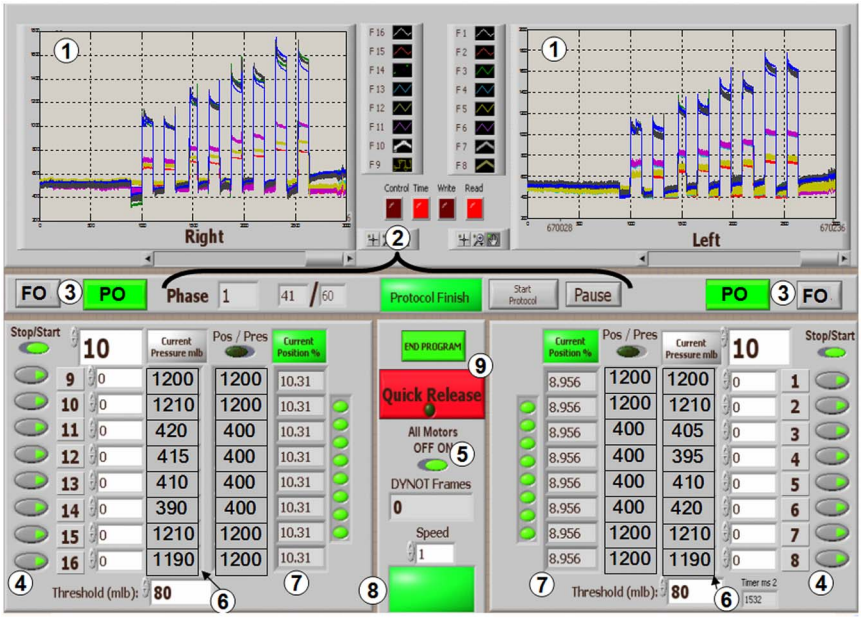

Fig. 3. (Color online) GUI of the sensing-head controller. See text for description.

readouts of periods within a protocol, and offsets for motor position and strain gauge reading (3). The elements of the lower panel provide for, among other features, manual control of individual motors (4) or for all motors at once (5), real-time readouts of strain (6) and motor position (7), and fields for specifying tolerance limits ["Threshold (mlb)"], synchrony with optical recordings, and motor target values. Also present is a subject-controlled safety display that turns red and reads "patient discomfort" when activated by the study participant (8), and an emergency release (9) that, upon activation, immediately returns the articulating units to their home positions, thereby releasing the breast.

System timing is under software control and operates nominally at 20 Hz. We are aware that software timing can lead to asynchronous operations involving the read, write, and update commands. However, because a precise time stamp is assigned to every event, hysteresis, if any, is precisely recorded. The impact of hysteresis is essentially insignificant, presenting only a small, but known, jitter in the sampling/control timing.

Because the direction, speed, and position of the motors and resulting magnitude of applied force are all under user control, a wide range of articulation maneuvers and timing sequences are available.

B. Illumination–Detection Scheme

The optical system and strategies for light detection and system timing are substantially similar to those of a previously described instrument [21]. Key elements include use of frequency encoding techniques, automated gain adjustment, and a time-multiplexing CW illumination scheme.

Briefly, thermoelectrically cooled laser diodes having spectral maxima at 760 and 830 nm were obtained from Intense, Ltd. and were modulated in the audio-frequency range using a Model 8000 Newport laser controller. Output of the laser diodes are combined into a single beam using a wave-division multiplexer obtained from OZ Optics, Inc., Canada. The combined source is optically coupled into a homemade optical switch comprising a high-capacity servo motor and a surrounding stator housing to which two parallel arrays of transmitting fibers (one for each breast) are mounted in a circular arrangement. Splitting of light into two parallel beams is achieved via a two-stage mirror assembly that is mounted to the top of the servo-motor shaft. In this fashion, light reflecting off the top and bottom mirrors is directed to one pair of receiving fibers. Motor movement repositions the mirror assembly, allowing for illumination of the next pair of fibers. Because motor repositioning is fast, the full scan across all 32 transmitting pairs of fibers provides for an image framing rate of approximately 2 Hz.

Signal detection is accomplished using silicon photodiodes that convert light intensity to electrical current with high quantum efficiency and signal-to-noise ratio. The dependence of photocurrent on input light intensity is linear over a broad range ($1:10^{10}$). To take full advantage of this range, we have introduced a two-stage programmable gain capability that supports signal amplification up to 10^6.

A lock-in detection circuit available on each detector channel is used to reduce electronic noise, eliminate interference from ambient light, and separate signals from the two optical sources. Parallel detection is achieved via sample-and-hold circuitry whose output is transmitted to one of four data acquisition cards having 16 bit resolution (National Instruments, Model USB-6033E). These boards also provide eight programmable digital input–output ports, which are used to trigger the sample-and-hold circuit, enable and disable the optical switch, encode the position of the optical switch, control the gain level in the programmable gain circuit in each board, and synchronize the operation of the detection unit and the articulating sensing head.

Synchronized to motor movement is an updating of gain settings that takes full advantage of the large dynamic range intrinsic to silicon photodiodes. The resulting dynamic range is approximately 10^9. This range supports parallel measures of CW light intensity that span distances ranging from colocated with the source to approximately 15 cm away. Sixty-four

channel detection units were obtained from NIRx Medical Technologies, Glen Head, New York.

3. METHODS

A. Subject Recruitment

Human studies were conducted under SUNY institutional review board protocol 99-093 and Brooklyn Hospital Center protocol 599. Eligible participants included women who were either not pregnant or not past their first trimester of pregnancy and were 21 to 75 years old.

B. Setup

Informed consent and a brief medical history were obtained from the research participants. Subjects were seated in a multiaxis chair positioned sufficiently close to the imager to allow for positioning of the lower array of the sensing heads along the inframammary fold (fifth–sixth rib) such that the most anterior aspect could make contact with the chest wall. This placement was chosen because it serves to comfortably support the breast while not imposing a mechanical stress that could result in venous congestion. In addition, to ensure subject comfort and to minimize the tendency for movement, adjustable supports for the arms and feet were employed.

Prior to final breast positioning, the top half of the sensor array was opened by adjusting the pivot assembly (item 4, Figs. 2(b) and 2(d)). Each breast was then positioned centrally onto the lower arrays, and a force-offset measurement was performed. Following this, the top array was lowered to within a few millimeters of the breast surface, followed by activating the stepper motors to apply a baseline contact force of 1.8 N. Depending on the particular breast contour, the orientation of each articulating unit was subsequently adjusted manually, as needed, to ensure that each assembly was positioned perpendicular to the surface of the breast. Throughout the process, the two mechanical support arms were oriented to hold each sensing head at an angle of ~20° with respect to the midline, thus ensuring no mechanical interference between the sensing heads.

Following this, an automated gain adjustment was performed that employs a decision algorithm that compares signal levels at all gain settings and selects the one that provides amplitudes within an appropriate sensing midrange (0.1–2 V). Experience has shown that breasts having cup sizes ranging from B through DD can be accommodated without undue undersampling resulting from incomplete contact with the array, and without excessive light attenuation.

C. Articulation Protocol

Following setup of the optomechanical sensing heads, a baseline measurement lasting approximately 10 min was performed. Next, a preselected force maneuver protocol was implemented. While we have explored implementation of a wide range of protocols that vary the number of articulating units applying force (1–8 units), the duration and magnitude of applied force, and the articulation timing sequence, here we have implemented the protocol outlined in Fig. 4, which provides for measures of stress relaxation. During Period 1, a two-step compression–relaxation cycle is implemented wherein first all eight articulating units are engaged until a specified target force is achieved (Event A1). At this point, feedback control disables the motors but retains their positions, allowing for stress relaxation to occur for a period of 1 min. This is followed by a two-step relaxation process wherein first the four most mediolateral (ML) elements are returned to baseline levels (Event B1), followed by the four most craniocaudal (CC) elements (Event C1). This is followed by a second time interval, in which only the ML elements are engaged (Event D1), followed by their relaxation (Event E1). For consistency, the durations of all intervals of constant applied force were fixed at 1 min. The entire protocol was then repeated (Period 2), with the difference that the change in applied force between baseline and final target value was doubled from 2.7 to 5.4 N (7.1 N final value). Motivating this protocol was the goal of exploring gross redistribution of blood within the breast under distinctly different loading and unloading conditions. Our hypothesis is that the occurrence of local pathology may markedly alter this response and hence yield different contrast features.

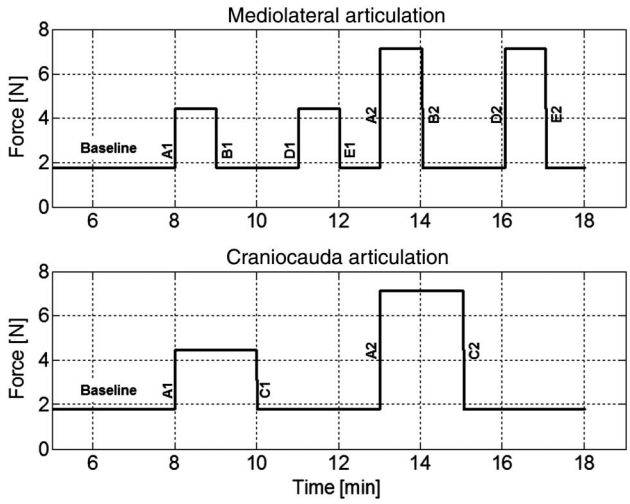

Fig. 4. Articulation protocol employed for clinical studies. The time-dependent target force of the ML and CC articulation units are identified. Two compression force values, 4.4 and 7.1 N, were applied.

D. System Performance Validation

System performance has been evaluated using laboratory phantoms that provide for objective assessment of both directly observable and recovered properties. The former were defined using a silicone-based phantom having an anthropomorphic form and adjusted to roughly approximate the optical properties of a breast. The latter were explored by introducing a programmable electrochromic cell (ECC), whose optical attenuation is voltage dependent, at a known location into a deformable balloon filled with 1% Intralipid, with or without added dye. These cells, having dimensions of the order of 1.5 cm × 1.5 cm × 0.2 cm, have a fast response and nearly 50-fold dynamic range. The use of these cells as a basis for developing programmable phantoms has been previously reported [34]. Images of these inclusions and their temporal dynamics are recovered from collected data.

Because the fidelity of recovered properties is a function of both system performance (optical and mechanical) and stability of the inversion algorithm, we have varied properties of the phantom to roughly span the range of parameters intrinsic to the natural variability of breast size and internal optical properties. In this way, we can directly test the stability of

the inversion algorithm to nonidealities originating from approximations in physical modeling and to a limited computational effort.

Photographs of the phantoms used in this study are shown in Figs. 2(a) and 5. The torso phantom shown in Fig. 2(a) is composed of silicone and doped with TiO_2 and dye to yield background optical properties of $\mu_s' = 8\,\mathrm{cm}^{-1}$ and $\mu_a = 0.1\,\mathrm{cm}^{-1}$. Here we have intentionally increased the absorption-coefficient value beyond what is typical of a breast of this size in order to require a large measurement dynamic range, as a means of testing the full range of system performance. The balloon phantom shown in Fig. 5 was used to test the impact that imposed deformations of the boundary, as a consequence of articulation, have on the recovered location and temporal dynamics of the included ECC. Additionally, to explore the influence of expected variability in breast size and composition, the volume of added Intralipid and the background absorption coefficient also were varied.

E. Data Processing

1. Viscoelastic Response

Coefficients of the viscoelastic response to applied force were determined by computing Young's modulus and the time constant for stress relaxation. Estimates of Young's modulus were computed using Hooke's law,

$$F = Ex, \tag{1}$$

where F is the applied force exerted on tissue (newtons), E is the elastic modulus or Young's modulus [pascals (Pa) ($1\,\mathrm{Pa} = 1\,\mathrm{N\text{-}m}^{-2}$)], and x is the deformation caused by applied force [meters (m)].

The time constants for stress-relaxation responses under conditions of loading and unloading were obtained using Maxwell's model [31,32], which considers an elastic spring and dashpot in series:

$$\sigma = Ex_0 \exp\left(-\frac{t}{\tau}\right), \qquad \tau = \frac{\eta}{E}, \tag{2}$$

where σ is the measured stress (Pa), $\sigma = F/A$, and A is the area of contact (m^2); E is Young's modulus (Pa); x_0 is the normalized initial deformation (dimensionless); t is time [seconds (s)]; τ is the time constant for stress relaxation (s); and η is the viscosity (Pa-s).

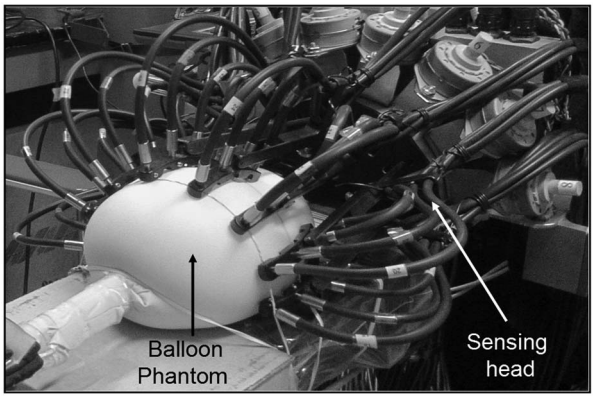

Fig. 5. Photograph of balloon phantom positioned within sensing head. The phantom contained India Ink and 1% Intralipid; an ECC was placed roughly in the center of the balloon to introduce dynamic changes in the optical properties.

2. Inversion of Optical Recordings

An elementary challenge to the recovery of useful hemodynamic parameters from optical measures of the breast, when the latter are related to articulation maneuvers that produce complex deformations of the boundary to an already mainly arbitrary shape, is the expected mismatch between true target properties and those of computational models. Standard linear perturbation theory is based on efforts that successively improve approximations between the computational model and the true target [14,35,36]. In cases where the goal is to obtain good estimates of the absolute background optical properties, experience has shown that consideration of the details of the boundary (both internal and external) is important. In practice, this would require adopting a computational model that takes into account the details of imposed deformations [37]. Even if such considerations were practical, the computational effort required to update the finite-element method (FEM) mesh and to perform recursive computations would be truly burdensome, especially for time-series studies. Fortunately, as we have shown in previous reports [38,39], if the goal is instead to characterize and localize relative changes in optical properties, adoption of complex computational models and techniques is not generally required.

F. Image Reconstruction and Calculation of Relative Changes in Hb Concentration

The application of a perturbation-based image reconstruction scheme derived from the radiation transport equation was introduced and explored by our group starting more than two decades ago [40,41].

Briefly, light propagation in scattering-dominant media such as breast tissue is well described by the diffusion process. For a spatial domain Λ with boundary $\delta\Lambda$, this can be represented by the expression

$$\nabla \cdot [D(\mathbf{r})\nabla\phi(\mathbf{r})] - \mu_a(\mathbf{r})\phi(\mathbf{r}) = -\delta(\mathbf{r} - \mathbf{r}_s), \qquad \mathbf{r} \in \Lambda, \tag{3}$$

where $\phi(\mathbf{r})$ is the photon density at position $\mathbf{r}$, $\mathbf{r}_s$ is the position of a CW point source, $D(\mathbf{r}) = 1/\{3[\mu_a(\mathbf{r}) + \mu_s'(\mathbf{r})]\}$ is the position-dependent diffusion coefficient, $\mu_a(\mathbf{r})$ is the position-dependent absorption coefficient, and the δ in the right-hand side denotes the Dirac delta function.

The forward problem is solved by use of an FEM with type III boundary conditions on a suitable model. The specific model considered here is shown in Fig. 6, contains 3908 nodes and 16,761 finite elements, and represents an approximation to the geometry of a typical breast when placed inside the sensing head. Indicated in red are the locations of optodes that

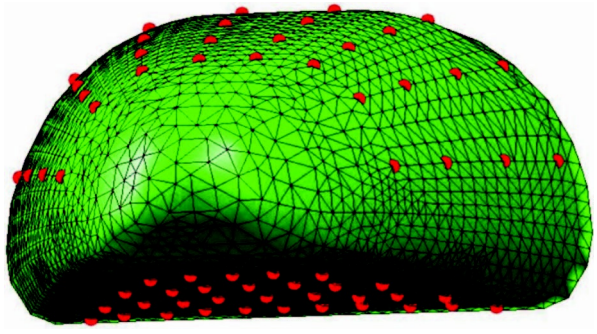

Fig. 6. FEM used for image reconstructions. Dots identify location of the optodes on the FEM surface.

coincide to a roughly D cup-size breast (physical dimensions of the model are 12 cm wide, 10 cm deep, 6 cm high) for which the sensing head is positioned against the chest wall. The optical coefficient values used to compute the reference medium were $\mu_a = 0.06\,\mathrm{cm}^{-1}$ and $\mu_s' = 10\,\mathrm{cm}^{-1}$ and were to selected to approximate those of human breast [42].

We cast the inverse problem in the form of a linear perturbation equation. This relates the difference between measured and predicted optical-signal levels at the surface to the difference between coefficient values of the true target and a specified reference medium:

$$\delta\mathbf{u} = \mathbf{W}_r\delta\mathbf{x}, \tag{4}$$

where $\delta\mathbf{u}$ is the vector of differences between the measured light intensity and that calculated for the reference medium, $\mathbf{W}_r$ is the Jacobian operator [14], and $\delta\mathbf{x}$ is the vector of differences between the optical properties $[\mu_a(\mathbf{r})$ and $\mu_s'(\mathbf{r})]$ of the target and the reference media.

The accuracy and reliability of the results obtained from Eq. (4) can be limited by many factors, such as errors in the measurement data and uncertainties in the reference model's boundary conditions. Our approach to minimizing the influence of these errors and uncertainties has been to evaluate relative instead of absolute light measures. Recasting Eq. (4) in accordance with this scheme, as outlined in [38], we get

$$\left[\frac{(\mathbf{u}_1)_i - (\mathbf{u}_2)_i}{(\mathbf{u}_2)_i}\right](\mathbf{u}_r)_i = \sum_j (\mathbf{W}_r)_{ij}(\delta\mathbf{x})_j, \tag{5}$$

where $(\mathbf{u}_1)_i$ and $(\mathbf{u}_2)_i$ represent any two measures of interest acquired at two different times for the ith source–detector pair; $(\mathbf{u}_r)_i$ and $(\mathbf{W}_r)_{ij}$ are the optical-signal level and Jacobian operator, respectively, computed for the reference medium; the summation in the right-hand side of Eq. (5) is over all area or volume elements considered by the image reconstruction. To compute the three-dimensional (3D) image time series of the wavelength-dependent absorption coefficient $\mu_a(\mathbf{r})$, we numerically solve Eq. (5) using the truncated singular value decomposition method, which is computationally efficient and regularizes the problem [43].

To transform the computed wavelength-dependent response into changes in Hb concentration, we solve a 2×2 system of linear equations [44]:

$$\begin{pmatrix}\delta[\mathrm{HbO}]\\ \delta[\mathrm{HbD}]\end{pmatrix} = \begin{bmatrix}\varepsilon_{\mathrm{HbO}}^{760} & \varepsilon_{\mathrm{HbD}}^{760}\\ \varepsilon_{\mathrm{HbO}}^{830} & \varepsilon_{\mathrm{HbD}}^{830}\end{bmatrix}^{-1}\begin{pmatrix}\delta\mu_a^{760}\\ \delta\mu_a^{830}\end{pmatrix}, \tag{6}$$

where $\varepsilon_{\mathrm{HbO}}^{760}$ and $\varepsilon_{\mathrm{HbD}}^{760}$ are the extinction coefficients for 760 nm light and $\varepsilon_{\mathrm{HbO}}^{830}$ and $\varepsilon_{\mathrm{HbD}}^{830}$ are the extinction coefficients for 830 nm light. The total Hb signal (HbT) is calculated as the algebraic sum of oxygenated Hb (HbO) and deoxygenated Hb (HbD) and the Hb oxygen saturation (HbSat) as the ratio of HbO to HbT.

4. RESULTS

A. System Operating Specifications

The principal operating specifications of the imager are summarized in Table 1. The optical system records from both breasts in parallel at a nominal image framing rate of 1.8 Hz when all 32 source positions are employed (i.e., 8192 sensing channels altogether, hence a 14.7 kHz data sampling rate).

Table 1. Mechanical and Optical Performance of Articulating Breast Imager

Type	Parameter	Value
Optical	Wavelengths	760 and 830 nm
	Number of Sources	64 (32 left and 32 right)
	Number of Detectors	128 (64 left and 64 right)
	Detector Sensitivity	10 pW
	Dynamic Range	$1:10^9$ (180 dB)
	Cross Talk (Optical)	$<1:10^{-5}$
	Cross Talk (Electronic)	$<1:10^{-6}$
	Long-Term Stability (40 min)	CV <0.3% up to gain 10^5, CV <2% at gain 10^6
	Dark Noise	<1 mV, up to gain 10^5, <7 mV, at gain 10^6
	Optical Data Acquisition Rate	1.8 Hz for 8192 channels
Mechanical	Force Sensitivity	0.04 N (0.01 lb)
	Capacity	15 N (3.4 lb)
	Cross Talk (Force)	$1:10^{-3}$
	Repeatability (STD)[a]	0.08 N (0.02 lb)
	Articulation Range	90 mm
	Articulation Speed	4.8 mm/s
	Mechanical Data Acquisition Rate	20 Hz for 16 channels

[a]STD, standard deviation.

Higher image framing rates are achievable by reducing the number of sources. Under the conditions considered for Table 1, each breast is illuminated by an array composed of 32 source positions and 64 detectors. The system has a nominal dynamic range of 10^9 and a detection limit of 10 pW. Optical-signal isolation (optical cross talk) at the level of the optical switch is $>10^5$ for adjacent illumination fibers. By adjusting incoming light power and the corresponding gain settings, it is possible to introduce widely different signal amplification values within the same dual-channel detector card. Measures showed that signal isolation (electronic cross talk) under these conditions is $>10^6$.

Key elements of the sensing head include performance of the stepper motors and strain gauges, mechanical limits, acquisition rates, and range of movement. The sensitivity of the strain gauges is 0.04 N, a value ~2% of the minimal contact force applied to the breast. This level of sensitivity greatly facilitates accurate measures of stress relaxation. The maximum force that can be applied, above which failure of the bond between the strain gauge and lever arm may occur, is 15 N. The design mechanics of the articulating units reduces the maximum force generated by the stepper motor from 100 N to an upper limit of 8 N applied to the breast. This value compares to forces in the range of 44–133 N that are employed in x-ray mammography studies [45]. Repeated articulation maneuvers applied to the silicone phantom, shown in Fig. 2(a), demonstrate that the applied-force precision is of the order of 1% of the maximum value (0.08 N).

A notable feature of the sensor head design is the range of movement. The 90 mm adjustment range for each articulation unit accommodates breasts that range in cup size from B to DD. The maximum speed of movement of the articulating unit at the level of the breast is determined by the update rate of the stepper motor (20 Hz), step size (0.0254 mm), and the design mechanics of the articulating unit assembly. In all, the

maximum movement rate achieved at the pivot point for the fiber holder is 4.8 mm-s^{-1}. Experience has shown that this speed is sufficient to achieve a force of 7 N within 2 s. Because each articulating unit can be controlled separately with high precision, protocols ranging from application of uniform force to directionally oriented fine articulation (e.g., medial progressing to lateral) that may serve to effectively "steer" the vascular response are feasible.

B. System Performance

1. Signal Stability

Dark Noise

Measurements of the mean dark noise, as a function of gain setting, for all source–detector pairs revealed that noise levels are below 1 mV for a sensing range of up to 10 V for gain amplifications up to 10^5. This value is <7 mV at gain amplification of 10^6. These values compare well with the performance of the first-generation system [21], and they are low relative to experimental signal values, which typically range from 0.2 to 2.0 V over the full range of gain settings for a size D breast.

Long-Term Signal Stability

Sources of noise that contribute to signal variance include fluctuations in laser power and variability in coupling of light through the two-staged optical switch. Estimates of their combined impact were assessed by computing the coefficient of variation (CV) from data collected from the breast-shaped phantom (size D, $\mu_s' = 8\,\mathrm{cm}^{-1}$, $\mu_a = 0.1\,\mathrm{cm}^{-1}$) under conditions of ambient light over a 40 min period. As listed in Table 1, the system's long-term CV is <0.3% for all gain levels, except the highest value, for signal levels of the order of 200 mV, and the CV value is of the order of 2% at the highest gain setting for similar signal amplitudes.

2. Recovered Temporal and Localization Accuracy of Dynamic Inclusions

Apart from the ability to impose precise articulation maneuvers on each breast, key to the imager's utility is the ability to accurately recover the location and temporal dynamics of a region of interest within the breast under the various conditions of manipulation. As pointed out above, the overall accuracy of the recovered features is a function of system performance (optical and mechanical) and the stability of the inversion algorithm to expected nonidealities caused by imposed surface deformations and the limited computational effort inherent to first-order solutions.

To explore the stability of the inversion algorithm to types of manipulations supported by the imager, we have conducted imaging studies using the balloon phantom described in Subsection 3.D containing a single ECC. The position of the included cell relative to the lower sensor array was fixed and was known to within 1 mm in all directions. The cell was driven using a 0.1 Hz square wave. Time-series imaging studies were performed using the same articulation protocol as employed in the clinical study (see Fig. 4) except that the maximum applied force was adjusted to yield surface deformations similar to those observed in the breast studies (up to 1 cm).

Shown in Fig. 7 is an exemplary result obtained following image reconstruction [Eq. (5)] using the FEM mesh shown in Fig. 6 and applied to the balloon phantom containing the ECC inclusion. In particular, the quantity plotted in Fig. 7 is the amplitude of the power spectral density (PSD) at 0.1 Hz, normalized to the maximum value, as a function of position. Inspection reveals that, despite differences in detail between the reference medium and true target, excellent localization of the cell's position is nevertheless achieved. This relative insensitivity to errors in boundary conditions is a noted feature of the image reconstruction technique that we have adopted [38].

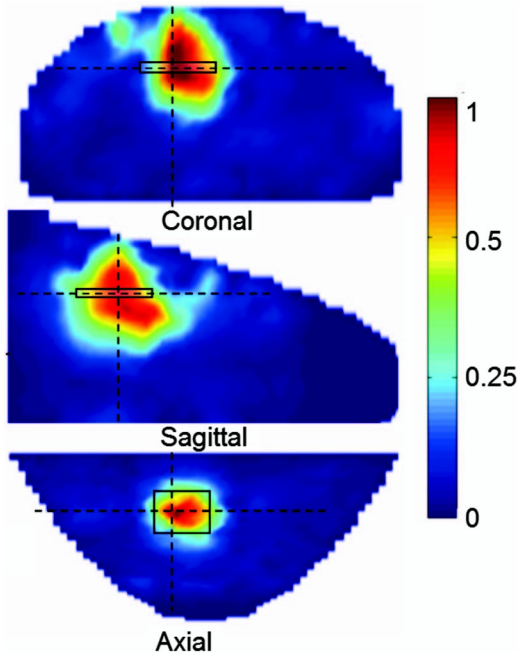

Fig. 7. 3D reconstructed image of balloon phantom. Axial, sagittal, and coronal cross-sectional images of the normalized PSD at 0.1 Hz computed from the reconstructed image time series of the 830 nm absorption coefficient. Rectangular elements represent the true location of the ECC.

Further evaluation of the performance of this inversion scheme under the expected articulation conditions is given in Table 2. Listed are measures of positional error and temporal fidelity [i.e., correlation (ρ) between the driving function and the reconstructed μ_a] of the recovered features as a function of the articulation protocol used in the clinical study. Positional error (millimeters) was determined by computing the center of mass of the recovered 0.1 Hz PSD at both illumination wavelengths and subtracting these from the known position of the ECC. Temporal fidelity was measured by computing the temporal correlation between the ECC square-wave driving function and the reconstructed dynamic response averaged over all pixels having 0.1 Hz PSD values within 50% of the maximum PSD.

Table 2. Accuracy Measures of Phantom Imaging Studies (Deformation Effects)

Condition	μ_{a760}		μ_{a830}	
	$(x-x_0, y-y_0, z-z_0)$	ρ	$(x-x_0, y-y_0, z-z_0)$	ρ
Baseline	(0, 3, –3)	0.97	(0, 1, –3)	0.99
Full Compression	(0, 0, –3)	0.94	(0, –1, –3)	0.96
ML Relaxation	(–1, 0, –3)	0.95	(–1, –2, –3)	0.95
CC Relaxation	(0, 0, –3)	0.94	(–1, –1, –3)	0.98
ML Compression	(1, 0, –4)	0.92	(2, –2, –5)	0.97

Table 3. Accuracy Measures of Phantom Imaging Studies (Effects of Size and Background Optical Properties)

Condition	μ_{a830} $(x-x_0, y-y_0, z-z_0)$	ρ
750 ml, 1 vol. % Intralipid[a]	$(0, +1, -3)$	0.99
750 ml, 1 vol. % Intralipid with India Ink	$(+2, 0, -2)$	0.97
1250 ml, 1 vol. % Intralipid	$(0, +2, 0)$	0.96
1250 ml, 1 vol. % Intralipid with India Ink	$(+2, +1, -2)$	0.94

[a]The medium contains 1% lipid by volume.

Inspection of Table 2 reveals that, excepting a modest bias in the recovered depth direction, accurate recovery of the cell's true position was obtained irrespective of the applied articulation or illuminating wavelength. Similar fidelity findings were obtained with regard to the accuracy of the recovered cell's temporal properties. In all cases, the recovered temporal correlation was in the range of 0.92–0.99, irrespective of the applied maneuver.

Table 3 shows results of similar studies, except that here the background absorption of the Intralipid solution and volume of the balloon were varied to reflect variability in associated parameters in a subject population. Absorption was adjusted by addition of India Ink to yield a final μ_a value of $0.06\,\mathrm{cm}^{-1}$. Also, balloon volume was increased from 750 ml (~D cup size) to 1250 ml (~DD cup size). Inspection shows that neither adjustment to the background absorption value or balloon volume significantly affected the accuracy of recovering the cell's location or its temporal properties.

Certainly, results of this quality could not be obtained if either the inversion algorithm were overly sensitive to distortions in the boundary (surface deformations, size) or to first-order errors in the initial guess of optical properties or if the quality of the measuring system (optical and mechanical) were in any way unstable. It deserves emphasis that, in a prior report [39], we have explored the ability to recover more complex spatiotemporal behaviors and obtained similar accuracy. We conclude that the system's overall capability (i.e., sensing, articulation, image recovery) is sufficiently robust to provide high confidence in equivalent measures performed on real breasts.

C. Clinical Study

In the following we outline some initial findings obtained using the described imager. In particular, a point made here is evidence of the scope of information that can be derived from concurrent optomechanical studies and evidence of the sensitivity of the method to the tumor phenotype.

1. Viscoelastic Response to Applied Force

Viscoelastic materials typically are explored under conditions that define either the time-dependent stress relaxation to a fixed deformation or the time-dependent deformation to a fixed applied stress (creep). While the imager is capable of implementing both types of protocols, here we focus on

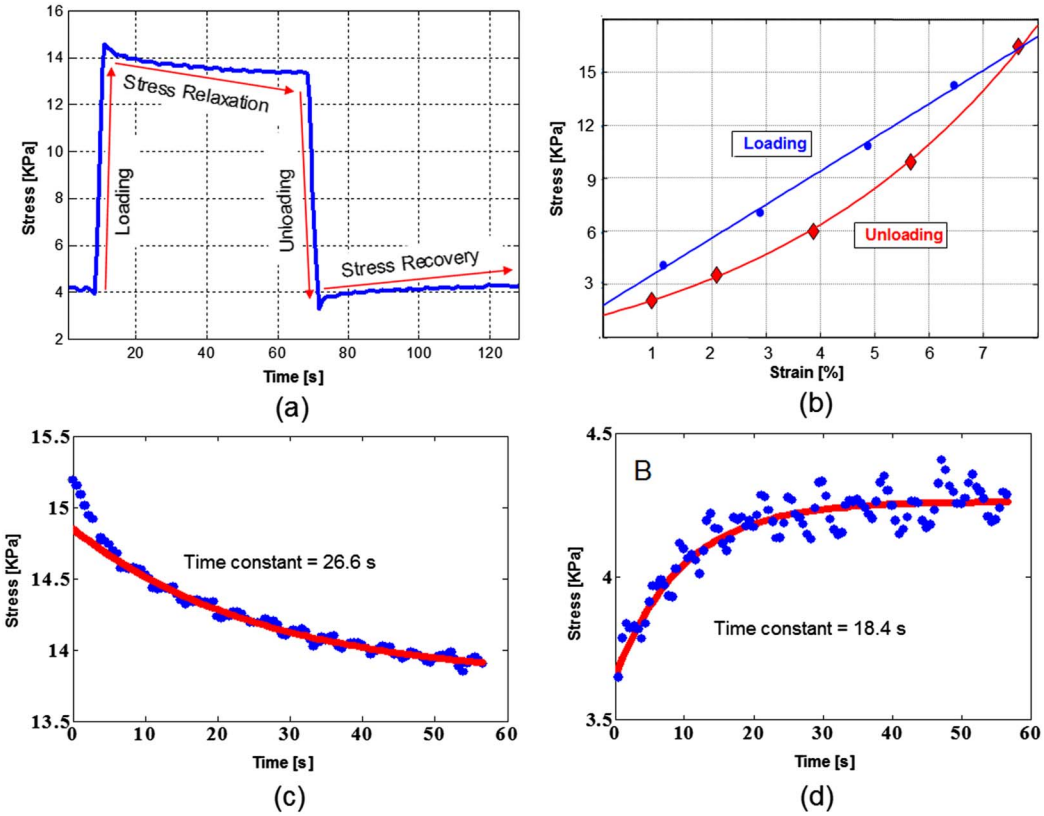

Fig. 8. (Color online) Viscoelastic response to applied force. Responses are from a lateral articulation unit in the left sensing head during application of 7.1 N of force. (a) Four phases of the applied protocol, (b) strain–stress relationship of the loading and unloading phases, (c), (d) stress relaxation and stress recovery (dots), respectively, and the corresponding best-fitting solutions to Maxwell's model (curves). Subject was 44 years old, healthy, with BMI of 23 and size D breasts.

Table 4. Sensitivity to Enhanced Stiffness in Tumor-Bearing Breast

		Orientation of Articulating Elements							
		Lateral		Craniocaudal				Medial	
Parameter		AU1[a]	AU2	AU3	AU4	AU5	AU6	AU7	AU8
Healthy Breast	Stiffness (kPa)	1.4	2.4	2.3	2.5	2.3	1.9	2.1	2.9
	Standard error	0.3	0.4	0.4	0.4	0.3	0.2	0.4	0.3
Tumor Breast	Stiffness (kPa)	1.7 [b]	2.1	2.2	2.3	2.4	2.4 [b]	2.8 [b]	3.5 [b]
	Standard error	0.3	0.2	0.4	0.3	0.4	0.3	0.3	0.2

[a]AU, articulating unit.
[b]These values are significantly different from the contralateral healthy breast (paired t-test, $p < 0.01$).

characterizing the breast response under fixed deformation conditions.

An example of the viscoelastic response observed during such maneuvers is shown in Fig. 8. Four phases are identified: loading, stress relaxation, unloading, and stress recovery [Fig. 8(a)]. Expanded views of these phases are shown in Figs. 8(b)–8(d). In Fig. 8(b) we have replaced the independent variable with measured strain. During the loading phase, the stress varies linearly with strain, which is the expected response of an elastic material as predicted by Hooke's law [Eq. (1)]. During unloading, stress varies in a distinctively nonlinear manner, a phenomenon characteristic of a viscoelastic medium and a finding that is consistent with prior studies on breast tissue [46,47]. Figure 8(c) shows the stress-relaxation response following loading, where a two-phase, time-dependent profile is seen. The slower response that begins at ~5 s after the end of the loading phase is well approximated by Maxwell's model of an elastic spring and dashpot in series (solid curve). We interpret this response as resulting from quasi-elastic decompression (stress relaxation) of the tissue scaffolding that comprises mainly elastin and collagen. The rapid phase immediately following loading we take as indicative of the response expected from vascular compression, in agreement with Carp *et al.* [28]. Shown in Fig. 8(d) is the response seen following the unloading period. Interestingly, the recovery profile seen here is monophasic and well approximated throughout its time course by Maxwell's model. Comparison of the derived time constants shows that a faster response is seen during the recovery period. We interpret this as the likely impact of vascular refilling.

2. Sensitivity to Enhanced Stiffness in Tumor-Bearing Breasts

Cancerous tumors are known to cause regional increases in tissue stiffness [48,49]. Two principal methods routinely adopted to support such detection are tactile sensing, as typically accomplished during the CBE, and elastography. Evidence that the articulating sensing head is sensitive to this phenomenology is shown in Table 4. Reported are stiffness values obtained under conditions of 7.1 N of force applied individually by each articulating unit, for a subject with a tumor-free breast and a breast containing a 2 cm diameter tumor in the upper outer quadrant (articulating units 6–8). The corresponding stiffness and standard error of regression were obtained by computing the slope of the linear strain–stress relationship [Eq. (1)] during the loading phase (among the eight articulating units, the correlation coefficient ranges from 0.997 to 0.999). It is seen that stiffness in the affected breast is significantly increased for four articulating units, three of which are in the vicinity of the tumor.

3. Stability to Subject Movement

Despite the comfortable seating afforded by the imager, it can be expected that some degree of subject movement will occur during the examination, which may serve to confound measurement findings. To explore this, we conducted a controlled study wherein a subject fitted with the dual-breast sensing heads was asked to undergo a set of specified movements. Shown in Table 5 is the measured change in the amplitude of the HbO signal during the course of the indicated maneuvers as compared to a resting baseline. Measured changes were calculated by determining the maximum range of response under the specified conditions, averaged over the entire sensing array. Note that, for ease of interpretation, values in Table 5 are normalized to the applied-force response (i.e., Range of change[%] = $100[\max(\mathrm{HbO}) - \min(\mathrm{HbO})]_{\mathrm{maneuver}}/[\max(\mathrm{HbO}) - \min(\mathrm{HbO})]_{7.1\ \mathrm{N\ compression}}$).

The "arm motion" data were collected while the subject raised and lowered her arms, from the waist to shoulder height, three times in succession; "speaking" data were collected while the subject read a text aloud for 1 min; "leg motion" data were collected while the subject raised first one leg and then the other to a height of six inches above the foot support three times in succession; and "head motion" involved slowly rotating the head from left to right, through a 90° angle, three times in succession.

Inspection of Table 5 reveals that the fluctuations associated with these movements are at least six times weaker than those associated with the indicated applied-force maneuver and are at most twice as strong as the fluctuations that occur during resting baseline conditions. We conclude that subject movement that may accompany the applied-force protocol does not significantly influence the quality of data associated with these maneuvers.

Table 5. Impact of Subject Movement on Optical Signal

Parameter	7.1 N Compression	Arms Motion	Speaking	Leg Motion	Head Motion	Baseline
Range of Change (%)	100	13.1	12.1	7.7	7.7	5.8
Standard Deviation	4.2	2.4	3.9	1.9	1.5	1.0

4. Measured Optical Response to Applied Force

Basic Considerations

In addition to imposing a viscoelastic response, articulation of the breast can be expected to provoke an optical-path-length change in a manner sensitive to tissue stiffness, as well as a hemodynamic response whose details will depend on the orientation of the sensing array with respect to the articulating elements. For instance, movement of the upper array elements can be expected to shorten the linear distance between these elements and the lower sensing array. With the applied forces considered here, in our experience this shortening can cause nearly a tenfold change in signal levels for some transmission-mode sensor arrangements. Also, given the known compliance of the venous circulation, even quite modest forces can be expected to cause some degree of venous congestion and thus modify details of blood flow. Thus, it can be anticipated that the response to applied force will involve both an optical-path-length change and a hemodynamic response.

While perhaps ultimately desirable, deconvolution of the effects of these two processes is not easily implemented. For instance, good estimates of the deformation of the tissue boundary can be extracted from known movements of the articulating elements, but the processing of this information would be burdensome and likely require recursive updates to the forward problem for each image frame in the time series. Instead, our approach here has been to limit the computational effort of the inverse problem to that outlined in Section 3.F.

As will be made clear below, adoption of this more limited analysis approach will produce hemodynamic findings that are convolved with path-length changes to different extents, depending on the orientation of the sensing elements. Nevertheless, as is outlined subsequently, we strongly believe that highly useful information still can be gleaned from the applied-force measures in a manner useful for the detection of tumors.

Exploration of Optical Subarrays

Optical changes in response to articulation that correspond mainly to a hemodynamic response can be expected to occur during periods of stress relaxation, at which times the entire sensing array is stationary, or at any time during the protocol period explored by the lower sensing array in the backreflection mode. Conversely, optical responses that are substantially convolved with a path-length change are limited to periods of active movement and involve transmission measurements.

Evidence of delineation of the indicated orientation-dependent optical/hemodynamic response to articulation is shown in Fig. 9. Depicted are the displacement (top panel) and hemodynamic response (lower panels) from a healthy volunteer undergoing the applied-force protocol outlined in Fig. 4. Recall that the protocol involves a series of full or partial compressions and subsequent unloadings, implemented at 2.7 and 5.4 N over the baseline contact force. For simplicity, the displacement response shown has been averaged across all articulating units. Inspection reveals that, as expected, applied force causes movement of the articulating units in an amplitude-dependent manner. Note that, upon full release

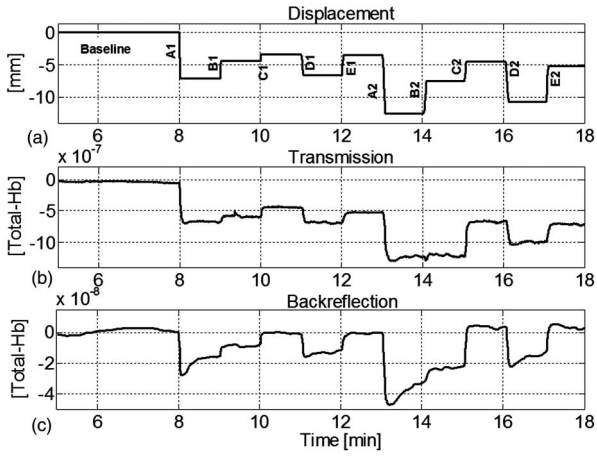

Fig. 9. Effect of articulation on optical signal. (a) Average displacement of all articulation units in the left sensing head; (b), (c) spatial mean of recovered time-varying total Hb molar concentration, derived from image time series reconstructed from only transmission data (b) or from only backreflection data (c). Plotted results are from the same subject as in Fig. 8.

of applied force, displacement does not return to baseline, indicating that some degree of tissue stretching has occurred.

Shown in the lower panels of Fig. 9 are the hemodynamic response of the HbT signal extracted from sensors that comprise either backreflection measures only or transmission measures only. Note that here we have identified the optical responses of subarray elements as an "apparent Hb" response in recognition of the limited data treatment. A gross inspection reveals that a notable difference between these two time tracings is the fact that the backreflection measures do fully return to baseline during periods of full release but those involving transmission measures do not and in fact are highly correlated with the displacement measures. A second observation is that the amplitude of the transmission response is nearly ten times greater than that of backreflection, a difference that is principally explained as the effect of a path-length change on the optical signal. Also seen is that, when force is applied, the amplitude of the Hb signal decreases in a force-dependent manner strongly suggestive of blood redistribution.

Certainly, our hope is that the manner in which such redistributions occur will be sensitive to the presence of pathology and can be further explored depending on the particulars of the articulation protocol. Appreciation of such details is limited in the tracings shown in Fig. 9 because the data presented were derived by computing the spatial means from a reconstructed image time series. A much richer depiction of the optical response to applied force is shown in subsequent figures, which are illustrative of reconstructed 3D images. Note that, in keeping with the above description, in the following we have computed images from data corresponding to transmission (Figs. 10 and 11) or backreflection (Figs. 12 and 13) only.

5. Optical-Signal Response to Applied Force

3D Image Response of Healthy Breast

Shown in Fig. 10 are axial, sagittal, and coronal cross sections derived from 3D HbT images reconstructed from data collected from a healthy volunteer [38 years old, body-mass index (BMI) of 33, size D breasts]. The positions of the planes

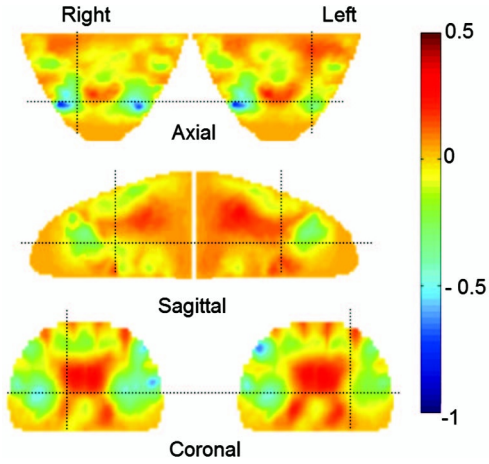

Fig. 10. 3D image response to applied force (healthy subject, transmission measures). The image is a representation of the applied-force dependence of the HbT concentration. The result is derived (see text for description) from image time series reconstructed from only transmission data. Articulation involved ML compression at 7.1 and 4.4 N. Data were obtained from a 38 year old subject with size D size breasts and BMI of 33.

relative to each other are identified by the dotted transects through the respective planes.

The quantity plotted in Fig. 10 is a linear combination of temporal-mean HbT images corresponding to four different 1 min time intervals: the 60 s periods immediately preceding and following the 2.7 N ML unloading (Fig. 4, Event E1) and the 60 s periods immediately preceding and following the 5.4 N ML unloading (Fig. 4, Event E2). Then the effect of the compressions on apparent HbT levels was assessed by computing the difference between the temporal-mean images for the first and second of the four 60 s intervals and likewise for the third and fourth intervals. Finally, the first difference was subtracted from the second in order to evaluate the pressure dependence of the apparent HbT response (i.e., $\Delta\Delta\mathrm{HbT}_{\mathrm{app}} = \Delta\mathrm{HbT}_{\mathrm{app}}^{5.4\,\mathrm{N}} - \Delta\mathrm{HbT}_{\mathrm{app}}^{2.7\,\mathrm{N}}$). (Note that, in order to generate a dimensionless quantity, which simplifies comparisons across subjects, the preceding difference of differences is normalized to its maximum absolute value in Fig. 10.)

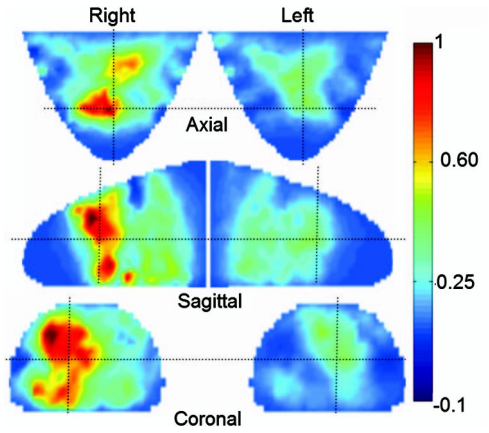

Fig. 11. 3D image response to applied force (tumor-bearing breast, transmission measures). Result of the same analysis as in Fig. 10 (see text for description) when applied to data obtained from a subject having a right-breast tumor. Articulation involved full compression at 7.1 and 4.4 N. The subject was 40 years old, with size D breasts, and BMI of 37 and had a 12 cm area of diffuse microcalcification (intraductal carcinoma) in the right breast.

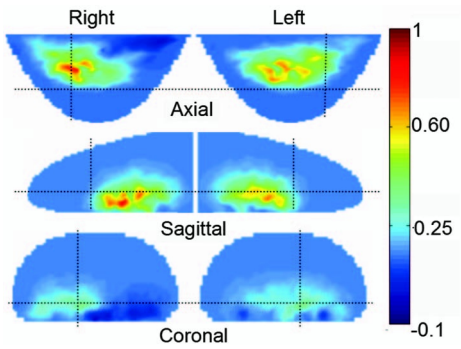

Fig. 12. 3D image response to stress relaxation (healthy subject, backreflection measures). The image is a representation of the average rate of change of the HbT concentration during a period of stress relaxation. The result is derived (see text for description) from image time series reconstructed from only backreflection data. Articulation involved full compression at 7.1 N followed by 60 s of stress relaxation. The subject was 44 years old with a BMI of 23 and size D breasts.

Inspection of Fig. 10 reveals three principal features. First, in regions where the optodes make direct contact with the tissue and whose articulating units undergo movement, a decrease in the apparent HbT levels is observed, particularly in the ML elements of the breast. This is quite reasonable as it is these areas that undergo the greatest deformation. Second, in the central region and along the superior boundary (see coronal section), an increase in the apparent HbT values is observed. This is also seems quite reasonable for two reasons. First, along the superior aspect of the breast, ML compression imposes an upwardly directed force sufficient to cause the articulating units to deflect slightly, thereby increasing the overall optical path length. Second, the applied force can be expected to divert blood from regions experiencing high force to low-force regions, causing a relative engorgement of the central elements of the breast, as seen.

The third evident feature is the striking similarity of the response in both breasts. The computed spatial correlations between the two breasts, for the image sections shown ranges from 0.85 to 0.87, indicating a substantially similar response. Inspection of the parent $\Delta\mathrm{HbT}_{\mathrm{app}}^{2.7\,\mathrm{N}}$ and $\Delta\mathrm{HbT}_{\mathrm{app}}^{5.4\,\mathrm{N}}$ responses (not shown) reveals that many of the contrast features seen in the difference-of-differences image are revealed upon application of the larger force, indicating a nonlinear effect.

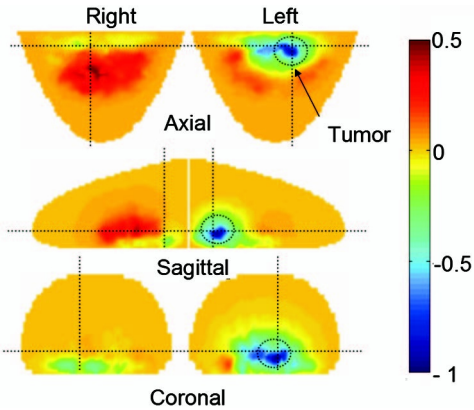

Fig. 13. 3D image response to stress relaxation (tumor-bearing breast, backreflection measures). Data analysis and articulation maneuver are the same as in Fig. 12 (see text for description). The subject was 50 years old with a BMI of 44 and size D breasts and had a 4 cm invasive ductal carcinoma at 4 o'clock in the left breast.

In contrast to the findings shown in Fig. 10, image features seen for a subject having a cancerous tumor and undergoing a substantially similar maneuver reveals a markedly different response.

3D Image Response of Tumor-Bearing Breast

Shown in Fig. 11 are results obtained for a force-unloading procedure similar to that used in the preceding healthy-breast case, except that here the applied force was generated by all of the articulating units. As in Fig. 10, the results represented are the difference (normalized to its maximum absolute value) between the apparent HbT responses seen at the two different levels of applied force.

The subject participating in this study (40 years old, BMI of 37, size D breast) had a diffuse infiltrating ductal carcinoma with microcalcification over a 12 cm area in the right breast. Inspection of Fig. 11 shows a diffuse high-contrast region in the right (affected) breast. As in the previous example, inspection of the parent responses (not shown) identified that much of the contrast revealed occurred at the higher applied-force magnitude. Apart from suggesting a nonlinear response to applied force (common to viscoelastic materials), these findings strongly indicate that the tumor-bearing breast has a higher intrinsic optical attenuation, possibly due to increased angiogenesis and to changes in the light scattering properties [50,51], thus contributing to the elevated contrast features revealed upon unloading compared to the unaffected contralateral breast.

6. Optical-Signal Response to Stress Relaxation

3D Image Response of Healthy Breast

Shown in Fig. 12 are the contrast features revealed during stress relaxation following loading of the breast to 5.4 N above the baseline contact force and recovered exclusively from the backreflection data recorded by the nonmoving bottom sensing array. As in Figs. 10 and 11, the positions of the planes relative to each other are identified by the dotted transects through the respective planes. As noted above, contrary to measures obtained from the moving array elements, here we believe that the majority of the contrast seen is unrelated to changes in optical path length and instead reveals responses closely tied to true changes in the Hb signal (i.e., $HbT_{app} \approx HbT$). The image feature plotted in Fig. 12 is the average slope of the HbT_{app} response, normalized to its maximum absolute value, seen during the 60 s stress-relaxation period immediately following the 5.4 N compression by all eight articulating units (i.e., the interval between Events A2 and B2 in Figs. 4 and 9).

Inspection of Fig. 12 reveals two prominent features. First is that, with few exceptions, the slope of the Hb signal is positive, indicating that, upon full compression, there is a net increase in blood volume in the lower aspect of the breast during stress relaxation. This response is reasonable given that the force is applied to the superior aspect and therefore diverts blood to areas of lower pressure. Interestingly, evidence of exclusion of Hb contrast is seen in the inferior elements of the breast (see sagittal view). Second, as in the previous findings from a healthy subject, the image features seen in the two breasts are substantially similar.

3D Image Response of Tumor-Bearing Breast

Shown in Fig. 13 are contrast features revealed during the period of stress relaxation in response to 5.4 N of loading force above baseline in the unaffected (right) and tumor-bearing (left) breast of a participant (50 years old, BMI of 44, breast size D) with a 4 cm diameter, invasive ductal carcinoma. As in Fig. 12, the specific feature plotted here is the normalized slope of the HbT_{app} response during the 60 s stress-relaxation period. Inspection reveals two prominent features. First is that the response of the unaffected breast is qualitatively similar to the response seen in the breasts of the healthy individual, i.e., pooling of blood in the inferior elements of the breast. Second is that, contrary to the unaffected breast, the tumor-bearing breast reveals a negative slope, indicating that Hb levels continue to decline throughout the period of stress relaxation. One plausible explanation for this divergent behavior is the expected influence of sluggish perfusion of the tumor vasculature. Because of enhanced resistance to blood flow, a delayed response can occur upon application of force. Additionally, increased stiffness could produce an aberrant viscoelastic response resulting in greater forces being translated to greater depths, which could lead to continued exclusion of blood during the period of stress relaxation [52]. It deserves noting that the findings represented as are meant only for illustrative purposes to document the basic sensitivity and capabilities of the imager. Results of an already completed systematic clinical investigation will be presented in a separate report.

To summarize, in this report we have described the system design features and performance characteristics of a simultaneous bilateral optical-viscoelastic measuring system that can explore the hemodynamic and optical-path-length changes seen during periods of loading and unloading and stress relaxation. System design provides for three independent concurrent measurements, optical, applied force, and displacement, and can support a wide range of protocols and breast sizes.

5. DISCUSSION

Central to optimization of imaging techniques for the detection of breast cancer is the adoption of sensing technologies inherently sensitive to key elements of the tumor phenotype. Two strategies widely adopted are use of tactile methods, principally accomplished as part of the CBE, and structural imaging methods. Representing a primary screening tool, the CBE employs both visual and mechanical inspection of the breast. Fundamental to this procedure is the understanding that the cancer phenotype produces distinctive changes in overall breast morphology, appearance, and physical properties that can be identified by skilled practitioners, while using a decidedly low-technology approach. Indeed, various reports have shown that between 4.6% to 10.7% of breast cancers detected in women who have undergone a screening mammogram are detected by CBE alone [53,54]. However, a notable limitation of the CBE is that it is essentially unsuited for detecting nonpalpable tumors. Detection of these tumors lies principally in the domain of imaging methods.

A key promise of the optical method follows from a recognition that principal features of the tumor phenotype, such as tumor angiogenesis, inflammation, and cellular dedifferentiation, will produce clinically useful contrast features that can

be revealed by spatial maps of wavelength-dependent optical coefficients, which can be used to identify naturally occurring components of the cellular milieu (e.g., Hb, water, lipid content) [55,56]. In recent years, our group has emphasized the added value of recording dynamic elements of tissue optical contrast that may naturally occur (e.g., natural beat frequencies associated with the vascular tree) or can be introduced through controlled manipulations [18–20]. By enabling high-density dynamic optical measures of the breast combined with concurrent viscoelastic measures explored through precise articulation, our goal here has been to capture the key elements of both strategies as a means for improved detection of breast cancer.

A. Contrast Mechanisms Associated with Applied-Force Maneuvers

Mechanical inspection of soft tissues is typically performed with the aim of defining the constitutive elements comprising the elastic response to an applied force. Two leading methods available to describe this response are US elastography [57] and MR elastography [58]. Techniques available to impose a mechanical force include quasi-static and vibratory compression. In principle, either paradigm can be considered to measure variables that are related to tissue stiffness, irrespective of the sensing technology (e.g., US or MRI). However, there are practical reasons why the former approach is preferred by developers of US elastography [57] and the latter by their MR elastography counterparts [5]. In the MR case, there is a well-posed image recovery problem, which confers an ability to accurately estimate the wavelength of the pressure wave at all points in a tissue structure. A mathematical formulation relating the experimentally determined wavelength to the local shear stiffness is used to compute an estimate of the latter quantity [5].

In contrast, the US elastography inverse problem is ill conditioned and susceptible to artifacts. In many cases, however, adequate levels of scientifically or clinically useful information can be extracted from relatively direct schemes, such as correlation analysis applied to US A-scans obtained at different levels of applied force. A limitation of the direct schemes is that the information that can be derived from them is limited to estimates of the position-dependent strain because stresses in the interior of the tissue structure are not directly measurable [57].

For both technologies, the amplitude of applied force is sufficiently small that induced deformations are $<1\%$ of the maximum tissue thickness. While the ability to impose substantially similar low-amplitude compressions in either a quasi-static or vibratory manner is possible with the sensing head developed here, our goal instead has been to impose compressions of much larger amplitude (5%–10%), not only for the purpose of supporting accurate external measures of elastic and viscous deformations but also to modulate the hemodynamic response. It is instructive to consider the contrast mechanisms that could be explored using large-amplitude quasi-static and vibratory methods.

B. Optomechanical Inspection of the Breast by Vibratory Compression

While not explicitly demonstrated here, the ability to achieve fine articulation without significant mechanical backlash in the sensing head does provide the ability to support protocols employing vibratory compression. Because our goal is to induce both a mechanical and a hemodynamic response, useful frequencies would likely be rather low, perhaps in the 0.1–1 Hz range.

1. Mechanical Response

Under low-frequency vibratory compression conditions, the dominant response to compression would be elastic. Unloading, however, would produce a nonlinear response due to the expected hysteresis associated with the time-dependent effects of tissue viscosity. Because the time constant of this relaxation process is likely longer than the period associated with these frequencies, repeated applications of force can be expected to induce tissue stretching, essentially a manifestation of creep. While not measured under precisely these conditions, the stepwise repeated applications of applied force shown in Fig. 9 provide direct evidence of this tissue stretching phenomenon. Also, while not detailed here, we have observed a heightened degree of tissue stretching in a number of tumor-bearing breasts, a finding that, at first consideration, seems paradoxical owing to the general tendency for greater stiffness in tumors. One possible explanation for this is the expectation of release of tumor metalloproteases in support of invasiveness, which has the effect of weakening extracellular elastin–collagen support structures [59,60].

2. Hemodynamic Response

The predominant hemodynamic response to applied force will be exclusion of blood from the breast, especially from the venous compartment. Refilling will occur with unloading but with added time delays stemming from the previously mentioned viscosity-induced hysteresis. An additional source of time delays would be the likely induction of vascular steal owing to variations in local pressure gradients, especially in the dorsal regions of the breast. In fact, in data not shown, we have seen evidence of this in quasi-static studies, most notably in the known vicinity of a tumor.

C. Optomechanical Response to Quasi-Static Compression

1. Mechanical Response

Quasi-static conditions directly support quantitative measures of the viscous response due to stress relaxation. Direct evidence that such measures can provide discriminatory information of the presence of tumors is shown in Fig. 13. As indicated, the ability to measure displacement to a fixed applied force also supports measures of creep. While both measures explore elements of viscosity, given the expected heterogeneity of a tumor-bearing breast it seems likely that there would be a differential response to the two types of mechanical relaxation processes.

Further discriminatory capabilities are likely accessible from implementation of more complex loading schemes. Reported here are results recorded from full-compression and ML-compression protocols. The noted ability for fine articulation readily supports additional protocols comprising propagating waves, whose effect would be to cause controlled steering of hemodynamics.

2. Hemodynamic Response

Compared to vibratory protocols, quasi-static loading conditions will likely support greater discrimination between the hemodynamic responses attributable to elastic and viscous deformations. As demonstrated here, the particulars of this differential response will vary with the details of the articulation protocol (e.g., full-compression, ML) and which elements of the subarray are explored (e.g., transmission versus backreflection).

In all, the expected interplay between controlled mechanical deformation and the ensuing hemodynamic response strongly argues in favor of the ability to access a wealth of differential contrast mechanisms. While such information is likely accessible, a key element in rendering this information useful is careful attention to feature extraction schemes that are tolerant to the mechanical deformations imposed. In fact, because measures of deformation and stress relaxation are recorded, specific measures of the elastic modulus and viscosity are available [see Eqs. (1) and (2)].

D. Approaches to Data Analysis

1. Analysis of Mechanical Data

Unlike purely elastic materials, viscoelastic materials have both elastic and viscous components. Viscosity produces a time dependence to the strain–stress response. Another phenomenon observable in the stress–strain curve is hysteresis, with the area of the hysteresis loop being equal to the energy lost during the loading cycle [46], and this lost energy is proportional to the viscosity coefficient of the tissue under test [see Fig. 8(b)]. With loading, a linear response to applied force is seen [Fig. 8(b)] underscoring the applicability of Hooke's law, even under strains that approached 10%–15%. In its simplest form, such responses can be interpreted as a linear compression of the vascular space, thus facilitating interpretation of models intended to extract hemodynamic features that are not directly observable [28]. During periods of stress relaxation, estimates of the boundary-dependent viscosity coefficient can be derived from fits to Maxwell's model. The same also applies to the recovery period following the unloading phase [Fig. 8(d)]. Although not presented here, we are aware that measures of creep can be well approximated by Voigt's model [32].

While the preceding represents information derived from direct measures of applied force and deformation, in contrast to the US and MR elastography imaging methods, this information does not, by itself, easily allow one to infer the internal constitutive mechanical properties of the breast. Rather, it has a flavor much more strongly in line with another mechanical inspection technique known as tactile imaging (TI) [61,62]. This method involves manually translating a mechanical force-sensing array across the tissue surface and measuring its reactive force. This FDA-approved technology is capable of performing a full examination of the breast, but, unlike MR and US elastography, it does not directly explore the depth dependence of tissue elasticity. In principle, inversion of reactive force measures is possible, but the associated computational overhead is considerable [62], and precise knowledge of the tissue boundary almost certainly would be required in order to obtain stable solutions. A limited depth dependence of the effective stiffness has been described using empirical techniques for TI studies [62].

By comparison, the general approach adopted here constitutes a hybrid of the established elastography imaging methods and TI. Similar to TI, we directly measure the reactive force. Likewise, similar to the elastography methods, we employ a penetrating energy source (i.e., NIR light) to record the effect of applied force. Thus far, our system design does not provide for surface tactile scans, but such capability could be introduced. Instead, specified articulation maneuvers are employed that support measures of creep and stress relaxation, in addition to measures of force transients. Compared to TI, a notable additional mechanical sensing capability introduced here is the associated measures of surface deformation.

As is discussed subsequently, we are aware that the superposition of information resulting from deformation and concurrent hemodynamic responses poses a challenge to attempts to separate such information using model-based imaging schemes of the type adopted here.

2. Analysis of Optical Data

Moving and Nonmoving Subarrays

As noted above, the application of force by the upper array will produce two principal optical responses (i.e., true hemodynamic and path-length changes), depending on whether the associated source–detector pairs have undergone movement or not. Measures independent of path-length changes are recorded by backreflection pairs housed in the stationary lower array. The depth to which such measures can reliably probe the tissue will vary depending on the optodes' separation distance. In our experience with many different tissue types, the maximum expected penetration by a backreflection measure is ~3 cm. It is for this reason that the images shown in Figs. 12 and 13 do not reveal contrast features lying deeper than one third of the way into the breast from the lower array. Substantially similar measures are available from optode pairs that affect a backreflection measurement in the upper array, whether or not the articulating units are moving. Consideration of all backreflection elements will support inspection of the optical response to the outer 3 cm of the breast. For sensitivity to greater depths, consideration of transmission measurements is required.

Data from optical transmission measurements performed in combination with applied force will almost certainly include a large effect stemming from changes in optical path length. Significantly, the amplitude of the path-length change can be expected to vary with the reactive force produced by the tissue. Regions of tissues having increased stiffness will undergo reduced deformation to a fixed applied force in comparison to regions that are more compliant. Strongly correlated with these changes will be variations in the amplitude of transmitted light. In our experience, it is not atypical to observe intensity changes of the order of tenfold for every centimeter of tissue deformation. The applied-force amplitude used here (up to 7.1 N) certainly can be expected to expel blood from the illuminated field. Thus, as noted, transmission measurements under conditions of applied force are sensitive to both path-length and hemodynamic changes.

Separation of these two responses, while desirable, is not straightforward. One significant challenge is the expectation that the spatial dependence of applied force will be significantly nonuniform throughout the breast. Highest values will

occur immediately under areas of tissue having direct contact with the sensing elements of the articulating units. Because a reactive force will be incurred along the caudal element of the sensing head, increased force will also be present in this region. In between, the magnitude of force will decrease, being lowest roughly in the middle [63]. As experimentally demonstrated by Darling *et al.* [52], the spatial dependence of this assignment can become complex, even for simply structured media containing a single region of increased stiffness.

Because reliable estimates of the linear distance between any two optodes are available from knowledge of the articulating units' positions (movement), estimates of partial separation of the two responses to applied force might prove possible. The idea here is that, using the indicated information, it should be possible to estimate the background optical properties of the breast based on the fits to diffusion solutions that make use of distance-dependent changes in intensity and of measures of the absolute light attenuation observed [64]. In the limit of small tissue deformations, changes in hemodynamics might be minimal while changes in optical path length are easily recorded. With greater deformation, associated changes in hemodynamics should become much more pronounced.

Inversion of Optical Data

As a first approximation, here we have employed the normalized difference method for reconstruction of 3D images [38] using an undeformed model. A notable feature of this method is its documented remarkable stability to expected errors in estimates of the boundary conditions and background optical properties [38,65]. In several reports we have previously documented that incomplete knowledge of internal optical properties, size of the target medium, inclusion contrast, etc., have little impact on the localizability of embedded inclusions and, importantly, on accurate recovery of even complex temporal dynamics [39]. The previously published findings are reinforced here by the studies performed on the balloon phantom. For simplicity, here we have also used a single reference medium (Fig. 6). In practice, given that our instrument can accommodate breast sizes ranging from B to DD (~300–1500 cm^3), use of models covering a range of sizes (e.g., small, medium, and large) might be warranted.

A straightforward consideration to documenting the effects that incomplete knowledge of boundary conditions has on the accuracy of recovered images is to perform studies on laboratory phantoms having an anthropomorphic form. Here we have extended our demonstration of the merits of adopting programmable phantoms that employ ECCs. In fact, the reconstructed image shown in Fig. 7, documenting excellent recovery of the spatial and temporal properties of the inclusions, was computed using the same FEM model (Fig. 6) as was employed for the representative clinical studies. Certainly, it is our hope that explicit consideration of individual details of deformation is not necessary in order to accurately recover at least the principal contrast mechanisms identified above. Our point in mentioning this, apart from its own merits for validating system performance, is that, while our emphasis here is appropriately directed primarily toward describing elements of system design and performance, we are aware of the need for greater attention to elements of data analysis. Ideally, inverse modeling would accurately account for the depressions in surface geometry incurred with applied force. We are aware that first-order solutions are prone to spatial biases, but, as identified in a series of reports, computationally efficient image correction strategies are available that appear to have promising performance [66]. We also note that the impact of breast deformation on inverse computations has been explored by Dehghani *et al.* [67], who observed that, while use of an undisturbed model does lead to artifacts, maps of absorption nevertheless are recovered with good performance.

Apart from particulars of image recovery, it also is appreciated that the considered applied-force maneuvers and the expected induced mixture of contrast mechanisms strongly lend the resulting data to analysis using signal separation methods that may be strongly or weakly model based [39,68,69]. A well-known example of the former is the general linear model. Use of this method seems highly appropriate given the availability of reactive stress and deformation measurements. Yet another method that would appear promising for separating physical from physiological responses is independent component analysis. Naturally, the point of applying these methods is to assist in isolating specific contrast mechanisms that are associated with key phenomenologies of the cancerous state. As noted, we believe our ability to employ a wide range of articulation maneuvers with high precision, while simultaneously recording optical (hemodynamic and pathlength effects), reactive strain, and deformation data, should allow for exploration of a host of potentially promising protocols that can serve to differentiate healthy from affected breasts. While not explicitly emphasized here, it is also worth noting that our capacity to perform simultaneous bilateral measures can be expected to add discriminatory power, given the explicit ability to regress out background physiological signals.

To the best of our knowledge, although many of the above-described attributes of optomechanical imaging are new, we note that our group was not the first to consider employing optical methods together with applied force. As summarized below, while four other groups have appreciated the potential utility, the implemented strategies are notably different from the approach described here [25–30].

E. Prior Applied-Force–Optical-Detection Methods for Studies of the Breast

Noting that all contact-based optical studies of the breast unavoidably result in some degree of applied force, Jiang *et al.* [25] explored its impact on components of the Hb signal and background scattering properties in the pendent breast. Interestingly, the sensing approach they adopted also allowed for measures of deformation, reactive force [in response to uniform stepped circumferential compression (up to 1200 Pa)], and optical tomographic studies (6 wavelengths). Three principal findings were obtained. Increased pressure significantly reduces tissue water content, presumably in response to interstitial water transport; increases tissue HbT and HbSat; and causes absorption and scattering changes that vary with BMI. The findings were interpreted as indicative of the expected dependence of water and Hb content on the extent of glandular tissue present. They concluded that added sensitivity to physiological and pathological states might be exploited from observed changes in functional information and elastic response.

In a subsequent report [26], with a larger number of subjects, the same group explored the kinetics of the optical response using a grossly similar measurement approach. Different here was the use of a reduced number of wavelengths with a faster framing rate and seemingly application of much greater compressions (up to 25 kPa). Under these conditions and contrary to their previous report, they observed that HbT levels declined with applied force, while tissue water and HbSat were unchanged. While no explicit reconciliation was given, it is noted that a different parameter estimation algorithm was employed for analysis of the optical data (method of spectral constraints) [70]. Also noted by the authors and similar to the present report, there was no explicit effort to account for surface deformation to applied force.

Using a more simplified measurement scheme and planar compression applied to a supported breast, Carp *et al.* [27,28] have studied directly measured and computed Hb metrics of the breast in response to applied force. Interestingly, the thrust of this study was an extension of the original suggestion made by Jiang *et al.* [25] as it relates to the possibility of deriving added physiological information from applied-force maneuvers. Here their focus was, in addition to direct measures of the Hb signal, to estimate changes in blood flow and tissue oxygen consumption using a particular algorithmic approach. Compared to findings by Jiang *et al.* [26], Carp *et al.* [28] observed that applied force produces both a decrease in HbT levels and HbSat. Precise reconciliation of these findings is difficult owing to differences in the amplitude and uniformity of applied force and, in particular, in the orientation of the breast.

As noted above, the optical sensing approach employed by Carp [27,28] is substantially similar to the measures achieved with our stationary lower array. Different is the amplitude of applied force (larger forces applied by Carp *et al.* [28]) and its uniformity. With regard to our findings, as noted, the time course of changes in the HbT signal that we observed are substantially similar to that reported by Carp *et al.* [28].

Yet another optical sensing approach with applied force has been considered by Athanasiou *et al.* [71]. This study explored the performance of a commercial optical breast imaging system to MR. The optical device examined employs a broad, nearly uniform illumination to the cranial surface of the breast while measuring the time-dependent optical response in transmission. Interestingly, soft compression of the breast with nearly uniform force (details not identified) was achieved by deforming a silicone membrane over the upper surface. Unlike results reported here and by the other groups [50,72,73], optical measures were restricted to a single wavelength (640 nm). In general, while evidence of sensitivity to the presence of cancerous tumors was demonstrated along with the suggestion of interesting differences in the dynamics between affected and unaffected regions, it was noted that the optical measure had a high rate of false-positive responses (32%) compared to negative MR controls.

Still another optical sensing approach with applied force has been reported by Xu and coworkers [29,30]. As noted by the authors, motivating their approach to optical breast studies has been appreciation that, whereas absolute easures of various breast-tissue characteristics definitely reveal differences between malignant breast lesions and normal breast tissue [50,56], the observed intrasubject and intersubject variances can be large and are affected by factors such as the patient's menopausal status [42]. By contrast, they have hypothesized that dynamic measures, corrected for baseline responses, could serve to minimize influences of tissue heterogeneity and interpatient variation. To this end, they developed a handheld multisensor optical device containing a reactive force sensor. Contrary to the above-mentioned studies and the current report, data collection under conditions of applied force were made in a manner similar to how a CBE is performed (i.e., breast unsupported and subject lying supine with ipsilateral arm overhead). Also different from the approach considered here is the need for prior knowledge of the location of a suspected lesion. Xu and coworkers [29,30] have reported that, using a ramped approach to applied force (up to 15 N), oxygen saturation and Hb content in affected regions were significantly lower than in unaffected regions.

To summarize, optical studies involving applied-force maneuvers have been made under conditions where the breast is unsupported [29,30], supported [27,28,71], and pendent [25,26]. These studies have involved ramped [25,26,29,30] and step maneuvers [27,28] and have involved optical measures comprising full tomographic [25,26], low sensor-density stationary backreflection [27,28], and higher sensor-density moving backreflection [29,30]. In each of these studies, the objective has been to employ applied force as a strategy for controlled provocation. By contrast, while we also adopt applied-force maneuvers as a means to provoke a physiological response, we believe it is important to specifically measure the mechanical response as well as to impose maneuvers in ways that support a broad range of protocols. Beyond this, and in keeping with our original description of the fundamental utility of dynamic NIR spectroscopic tomography [16,17], we believe that the capacity to account for intrinsic responses by involving simultaneous bilateral breast measures should serve to improve the diagnostic potential of any given protocol.

A summary of the considered capabilities as they relate to existing methodologies for breast cancer detection is shown in Fig. 14. Expression of the cancer phenotype produces measurable changes in the structural, functional, and mechanical

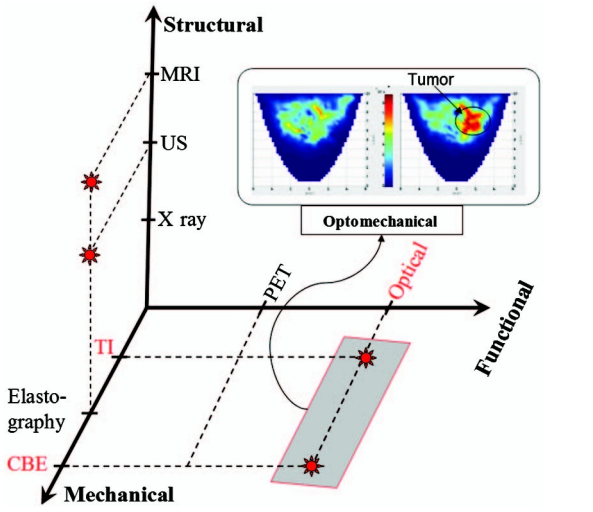

Fig. 14. Sensing domains for breast cancer detection. Optomechanical image shows region of enhanced contrast and tumor location due to applied force.

properties of the breast. The highest spatial resolution is afforded by structural imaging methods. Each has its particular practical advantages, but, more often than not, distinguishable contrast features become apparent only when tumors are already well established.

Building on the premise that functional changes precede structural, functional imaging methods [e.g., positron emission tomography (PET)] fundamentally support tumor detection based on changes in the molecular machinery in the tissue milieu. Naturally, the utility of optical methods is based on the expectation that such changes impact wavelength-dependent absorption or scattering properties of tissue. While evidence has been presented that such changes do yield promising clinical sensitivity and specificity [50,72,73], the fact is that, compared to the structural imaging methods, the optical methods suffer from decidedly low spatial resolution.

Supported both by its simplicity and general reliability, mechanical inspection methods, in particular those employed in the CBE, are still another useful independent methodology for breast cancer detection.

Previously noted is the notion that efforts to convolve one sensing domain onto another can yield either additive or wholly new information depending on whether one domain interacts with the other. As identified in Fig. 14, the merging of mechanical and structural sensing domains has led to the introduction of elastography. In both instances, because the domains interact, wholly new contrast mechanisms are available. A similar consideration of merging of sensing domains has been adopted here for the purpose of assessing new contrast features. A key difference between these two approaches, however, is that whereas the information space of structural imaging is principally bounded by the relatively constant tissue contrast and composition, functional measures, specifically NIRS, are sensitive to a much larger information space including the effects of maneuvers (e.g., mechanical, respiratory gases, pharmacological, injected dyes) and their impact on associated contrast mechanisms (HbSat, HbT, path length, light scatter, etc.).

F. Future Directions

Central to the potential clinical utility of optomechanical studies of the breast is the optimization of protocols and use of sufficiently stable and accurate modeling techniques. Ideally, such studies would be guided by a clear understanding of the internal force distribution. Such information depends in a complex manner on the details of applied force and the constitutive mechanical properties of the breast [45,52]. A brief consideration of the required information space might suggest that the problem is simply too unstable to expect reliable outcomes. Without minimizing the basic complexity, evidence for optimism comes from two simple observations. The first is that what is being considered is derived from well-established phenotypes, and clinical experience has shown that measures closely tied to these are obviously useful. Second is the expectation that sensible use of referencing strategies, such as a comparison of findings for the suspected affected and unaffected breasts, or referencing techniques within a breast [29,30] should also prove useful. Yet another proven strategy is the use of multiple differential indicators to enhance clinical utility [30,74]. Finally, given that breast volume can vary of the order of a factor of ten and has a noted age dependence in its composition and rigidity, it seems likely that, whatever useful differential indicators are identified, these should be sensibly categorized in accordance to such principal characteristics.

ACKNOWLEDGMENTS

This research was supported by the National Institutes of Health (NIH) grant R41CA096102, the U.S. Army grant DAMD017-03-C-0018, the Susan G. Komen Foundation, the New York State Department of Health (Empire Clinical Research Investigator Program), the New York State Foundation for Science, Technology and Innovation—Technology Transfer Incentive Program (NYSTAR-TIPP) grant C020041, and NIRx Medical Technologies. The authors wish to acknowledge technical support from members of the NIRx team: Christoph Schmitz and Yaling Pei. Some of the devices used in this research are products of NIRx Medical Technologies, LLC.

REFERENCES

1. A. Jemal, R. Siegel, J. Q. Xu, and E. Ward, "Cancer statistics, 2010," CA Cancer J. Clin. **60**, 277–300 (2010).
2. R. E. Hendrick, "Contrast agents in breast magnetic resonance imaging," in *Breast MRI, Fundamentals and Technical Aspects* (Springer, 2008), Chap. 8, pp. 113–134.
3. P. Vaupel, F. Kallinowski, and P. Okunieff, "Blood flow, oxygen and nutrient supply, and metabolic microenvironment of human tumors: a review," Cancer Res. **49**, 6449–6465 (1989).
4. P. Vaupel, "Blood perfusion and microenvironment of human tumors, implications for clinical radiooncology," in *Tumor Blood Flow*, M. Molls and P. Vaupel, eds. (Springer, 2000) pp. 41–45.
5. A. Manduca, T. E. Oliphant, M. A. Dresner, J. L. Mahowald, S. A. Kruse, E. Amromin, J. P. Felmlee, J. F. Greenleaf, and R. L. Ehman, "Magnetic resonance elastography: non-invasive mapping of tissue elasticity," Med. Image Anal. **5**, 237–254 (2001).
6. A. L. McKnight, J. L. Kugel, P. J. Rossman, A. Manduca, L. C. Hartmann, and R. L. Ehman, "MR elastography of breast cancer: preliminary results," Am. J. Roentgenol. **178**, 1411–1417 (2002).
7. I. Blickstein, R. Goldchmit, S. D. Strano, R. D. Goldman, and N. Barzili, "Echogenicity of fibroadenoma and carcinoma of the breast. Quantitative comparison using gain-assisted densitometric evaluation of sonograms," J. Ultrasound Med. **14**, 661–664 (1995).
8. I. Céspedes, J. Ophir, H. Ponnekanti, and N. Maklad, "Elastography: elasticity imaging using ultrasound with application to muscle and breast *in vivo*," Ultrason. Imag. **15**, 73–88 (1993).
9. A. Evans, P. Whelehan, K. Thomson, D. Mclean, K. Brauer, C. Purdie, L. Jordan, L. Baker, and A. Thompson, "Quantitative shear wave ultrasound elastography: initial experience in solid breast masses," Breast Cancer Res. **12**, R104 (2010).
10. O. Warburg, F. Wind, and E. Negelein, "The metabolism of tumors in the body," J. Gen Physiol. **8**, 519–530 (1927).
11. E. L. Rosen, W. B. Eubank, and D. A. Mankoff, "FDG PET, PET/CT, and breast cancer imaging," Radiographics **27**, S215–S229 (2007).
12. S. S. Gambhir, "Molecular imaging of cancer with positron emission tomography," Nat. Rev. Cancer **2**, 683–693 (2002).
13. T. Durduran, R. Choe, J. P. Culver, L. Zubkov, M. J. Holboke, J. Giammarco, B. Chance, and A. G. Yodh, "Bulk optical properties of healthy female breast tissue," Phys. Med. Biol. **47**, 2847–2861 (2002).
14. R. L. Barbour, H. L. Graber, Y. Wang, J. Chang, and R. Aronson, "A perturbation approach for optical diffusion tomography using continuous-wave and time-resolved data," Proc. SPIE **IS11**, 87–120 (1993).
15. S. Srinivasan, B. W. Pogue, S. Jiang, H. Dehghani, C. Kogel, S. Soho, J. J. Gibson, T. D. Tosteson, S. P. Poplack, and K. D. Paulsen, "*In vivo* hemoglobin and water concentrations, oxygen

saturation, and scattering estimates from near-infrared breast tomography using spectral reconstruction," Acad. Radiol. **13**, 195–202 (2006).
16. R. L. Barbour, H. L. Graber, C. H. Schmitz, Y. Pei, S. Zhong, S.-L. S. Barbour, S. Blattman, and T. Panetta, "Spatio-temporal imaging of vascular reactivity by optical tomography," in *Proceedings of Inter-Institute Workshop on In Vivo Optical Imaging at the NIH*, A. H. Gandjbakhche, ed. (Optical Society of America, 1999) pp. 161–166.
17. R. L. Barbour, H. L. Graber, Y. Pei, S. Zhong, and C. H. Schmitz, "Optical tomographic imaging of dynamic features of dense-scattering media," J. Opt. Soc. Am. A **18**, 3018–3036 (2001).
18. G. S. Landis, T. F. Panetta, S. B. Blattman, H. L. Graber, Y. Pei, C. H. Schmitz, and R. L. Barbour, "Clinical applications of dynamic optical tomography in vascular disease," Proc. SPIE **4250**, 130–141 (2001).
19. A. Y. Bluestone, G. Abdoulaev, C. H. Schmitz, R. L. Barbour, and A. H. Hielscher, "Three-dimensional optical tomography of hemodynamics in the human head," Opt. Express **9**, 272–286 (2001).
20. C. H. Schmitz, H. L. Graber, and R. L. Barbour, "Peripheral vascular noninvasive measurements," in *Encyclopedia of Medical Devices and Instrumentation*, 2nd ed., J. G. Webster, ed. (Wiley-Interscience, 2006), pp. 234–252.
21. C. H. Schmitz, D. P. Klemer, R. E. Hardin, M. S. Katz, Y. Pei, H. L. Graber, M. B. Levin, R. D. Levina, N. A. Franco, W. B. Solomon, and R. L. Barbour, "Design and implementation of dynamic near-infrared optical tomographic imaging instrumentation for simultaneous dual-breast measurements," Appl. Opt. **44**, 2140–2153 (2005).
22. Q. Fang, S. A. Carp, J. Selb, G. Boverman, Q. Zhang, D. B. Kopans, R. H. Moore, E. L. Miller, D. H. Brooks, and D. A. Boas, "Combined optical imaging and mammography of the healthy breast: optical contrast derived from breast structure and compression," IEEE Trans. Med. Imaging **28**, 30–42 (2009).
23. Q. Zhu, P. U. Hegde, A. Ricci, M. Kane, E. B. Cronin, Y. Ardeshirpour, C. Xu, A. Aguirre, S. H. Kurtzman, P. J. Deckers, and S. H. Tannenbaum, "Early-stage invasive breast cancers: potential role of optical tomography with US localization in assisting diagnosis," Radiology **256**, 367–378 (2010).
24. B. Brooksby, B. W. Pogue, S. Jiang, H. Dehghani, S. Srinivasan, C. Kogel, T. Tosteson, J. B. Weaver, S. P. Poplack, and K. D. Paulsen, "Imaging breast adipose and fibroglandular tissue molecular signatures using hybrid MRI-guided near-infrared spectral tomography," Proc. Natl. Acad. Sci. USA **103**, 8828–8833 (2006).
25. S. Jiang, B. W. Pogue, K. D. Paulsen, C. Kogel, and S. P. Poplack, "*In vivo* near-infrared spectral detection of pressure-induced changes in breast tissue," Opt. Lett. **28**, 1212–1214 (2003).
26. S. Jiang, B. W. Pogue, A. M. Laughney, C. A. Kogel, and K. D. Paulsen, "Measurement of pressure-displacement kinetics of hemoglobin in normal breast tissue with near-infrared spectral imaging," Appl. Opt. **48**, D130–D136 (2009).
27. S. A. Carp, T. Kauffman, Q. Fang, E. Rafferty, R. Moore, D. Kopans, and D. A. Boas, "Compression-induced changes in the physiological state of the breast as observed through frequency domain photon migration measurements," J. Biomed. Opt. **11**, 064016 (2006).
28. S. A. Carp, J. Selb, Q. Fang, R. Moore, D. B. Kopans, E. Rafferty, and D. A. Boas, "Dynamic functional and mechanical response of breast tissue to compression," Opt. Express **16**, 16064–16078 (2008).
29. R. X. Xu, D. C. Young, J. J. Mao, and S. P. Povoski, "A prospective pilot clinical trial evaluating the utility of a dynamic near-infrared imaging device for characterizing suspicious breast lesions," Breast Cancer Res. **9**, R88 (2007).
30. B. Wang, S. P. Povoski, X. Cao, D. Sun, and R. X. Xu, "Dynamic schema for near infrared detection of pressure-induced changes in solid tumors," Appl. Opt. **47**, 3053–3063 (2008).
31. R. M. Christensen, "Viscoelastic stress strain constitutive relations," in *Theory of Viscoelaticity*, 2nd ed. (Academic, 1982), Chap. 1, pp. 16–20.
32. R. Lakes, "Constitutive relations," in *Viscoelastic Materials* (Cambridge University, 2009), Chap. 2, pp. 22–26.
33. P. Regnault, "Breast ptosis: definition and treatment," Clin. Plast. Surg. **3**, 193–203 (1976).
34. R. L. Barbour, R. Ansari, R. Al abdi, H. L. Graber, M. B. Levin, Y. Pei, C. H. Schmitz, and Y. Xu, "Validation of near infrared spectroscopic (NIRS) imaging using programmable phantoms," Proc. SPIE **6870**, 687002 (2008).
35. S. R. Arridge and J. C. Hebden, "Optical imaging in medicine: II. Modelling and reconstruction," Phys. Med. Biol. **42**, 841–853 (1997).
36. V. Ntziachristos, A. H. Hielscher, A. G. Yodh, and B. Chance, "Diffuse optical tomography of highly heterogeneous media," IEEE Trans. Med. Imaging **20**, 470–478 (2001).
37. F. S. Azar, D. N. Metaxas, and M. D. Schnall, "Methods for modeling and predicting mechanical deformation of the breast under external perturbation," Med. Image Anal. **6**, 1–27 (2002).
38. Y. Pei, H. L. Graber, and R. L. Barbour, "Influence of systematic errors in reference states on image quality and on stability of derived information for DC optical imaging," Appl. Opt. **40**, 5755–5769 (2001).
39. H. L. Graber, Y. Pei, and R. L. Barbour, "Imaging of spatiotemporal coincident states by DC optical tomography," IEEE Trans. Med. Imaging **21**, 852–866 (2002).
40. R. L. Barbour, H. L. Graber, R. Aronson, and J. Lubowsky, "Model for 3-D optical imaging of tissue," in *Proceedings of the 10th Annual International Geoscience and Remote Sensing Symposium* (IEEE, 1990), Vol. 2, pp. 1395–1399.
41. R. L. Barbour, H. L. Graber, J. Lubowsky, and R. Aronson, "Monte Carlo (MC) modeling of photon transport in tissue (PTT) V: model for 3-D optical imaging of tissue," Biophys. J. **57**, p. 382a (1990).
42. B. W. Pogue, S. Jiang, H. Dehghani, C. Kogel, S. Soho, S. Srinivasan, X. Song, T. D. Tosteson, S. P. Poplack, and K. D. Paulsen, "Characterization of hemoglobin, water, and NIR scattering in breast tissue: analysis of intersubject variability and menstrual cycle changes," J. Biomed. Opt. **9**, 541–552 (2004).
43. Y. Pei, H. L. Graber, and R. L. Barbour, "A fast reconstruction algorithm for implementation of time-series DC optical tomography," Proc. SPIE **4955**, 236–245 (2003).
44. J. Choi, M. Wolf, V. Toronov, U. Wolf, C. Polzonetti, D. Hueber, L. P. Safonova, R. Gupta, A. Michalos, W. Mantulin, and E. Gratton, "Noninvasive determination of the optical properties of adult brain: near-infrared spectroscopy approach," J. Biomed. Opt. **9**, 221–229 (2004).
45. D. G. Russell and J. T. Ziewacz, "Pressures in a simulated breast subjected to compression forces comparable to those of mammography," Radiology **194**, 383–387 (1995).
46. A. Samani, J. Zubovits, and D. Plewes, "Elastic moduli of normal and pathological human breast tissues: an inversion-technique-based investigation of 169 samples," Phys. Med. Biol. **52**, 1565–1576 (2007).
47. J. Sciarretta, "MR validation of soft tissue deformation as modeled by non-linear finite element analysis," MS thesis (University of Toronto, 2000).
48. S. Kumar and V. M. Weaver, "Mechanics, malignancy, and metastasis: the force journey of a tumor cell," Cancer Metastasis Rev. **28**, 113–127 (2009).
49. P. Schedin and P. J. Keely, "Mammary gland ECM remodeling, stiffness, and mechanosignaling in normal development and tumor progression," Cold Spring Harb. Perspect. Biol. **3**, a003228 (2011).
50. R. Choe, S. D. Konecky, A. Corlu, K. Lee, T. Durduran, D. R. Busch, S. Pathak, B. J. Czerniecki, J. Tchou, D. L. Fraker, A. DeMichele, B. Chance, S. R. Arridge, M. Schweiger, J. P. Culver, M. D. Schnall, M. E. Putt, M. A. Rosen, and A. G. Yodh, "Differentiation of benign and malignant breast tumors by *in-vivo* three-dimensional parallel-plate diffuse optical tomography," J. Biomed. Opt. **14**, 024020 (2009).
51. S. Thomsen and D. Tatman, "Physiological and pathological factors of human breast disease that can influence optical diagnosis," Ann. N.Y. Acad. Sci. **838**, 171–193 (1998).
52. A. L. Darling, P. K. Yalavarthy, M. M. Doyley, H. Dehghani, and B. W. Pogue, "Interstitial fluid pressure in soft tissue as a result of an externally applied contact pressure," Phys. Med. Biol. **52**, 4121–4136 (2007).

53. S. McDonald, D. Saslow, and M. H. Alciati, "Performance and reporting of clinical breast examination: a review of the literature," CA Cancer J. Clin. **54**, 345–361 (2004).
54. J. J. Fenton, M. B. Barton, A. M. Geiger, L. J. Herrinton, S. J. Rolnick, E. L. Harris, W. E. Barlow, L. M. Reisch, S. W. Fletcher, and J. G. Elmore, "Screening clinical breast examination: how often does it miss lethal breast cancer?" J. Natl. Cancer Inst. Monogr. **35**, 67–71 (2005).
55. B. Brooksby, B. W. Pogue, S. Jiang, H. Dehghani, S. Srinivasan, C. Kogel, T. D. Tosteson, J. Weaver, S. P. Poplack, and K. D. Paulsen, "Imaging breast adipose and fibroglandular tissue molecular signatures by using hybrid MRI-guided near-infrared spectral tomography," Proc. Natl. Acad. Sci. USA **103**, 8828–8833 (2006).
56. S. Srinivasan, B. W. Pogue, S. Jiang, H. Dehghani, C. Kogel, S. Soho, J. J. Gibson, T. D. Tosteson, S. P. Poplack, and K. D. Paulsen, "Interpreting hemoglobin and water concentration, oxygen saturation, and scattering measured *in vivo* by near-infrared breast tomography," Proc. Natl. Acad. Sci. USA **100**, 12349–12354 (2003).
57. J. Ophir, S. K. Alam, B. Garra, F. Kallel, E. Konofagou, T. Krouskop, and T. Varghese, "Elastography: ultrasonic estimation and imaging of the elastic properties of tissues," Proc. Inst. Mech. Eng. H **213**, 203–233 (1999).
58. R. Sinkus, K. Siegmann, T. Xydeas, M. Tanter, C. Claussen, and M. Fink, "MR elastography of breast lesions: understanding the solid/liquid duality can improve the specificity of contrast-enhanced MR mammography," Magn. Reson. Med. **58**, 1135–1144 (2007).
59. B. Davies, D. W. Miles, L. C. Happerfield, M. S. Naylor, L. G. Bobrow, R. D. Rubens, and F. R. Balkwill, "Activity of type IV collagenases in benign and malignant breast disease," Br. J. Cancer **67**, 1126–1131 (1993).
60. M. Egeblad, M. G. Rasch, and V. M. Weaver, "Dynamic interplay between the collagen scaffold and tumor evolution," Curr. Opin. Cell Biol. **22**, 697–706 (2010).
61. P. S. Wellman, E. P. Dalton, D. Krag, K. A. Kern, and R. D. Howe, "Tactile imaging of breast masses," Arch. Surg. **136**, 204–208 (2001).
62. V. Egorov and A. P. Sarvazyan, "Mechanical imaging of the breast," IEEE Trans. Med. Imag. **27**, 1275–1287 (2008).
63. H. Ponnekanti, J. Ophire, and I. Cespedes, "Axial stress distribution between coaxial compressors in elastography: an analytical model," Ultrasound Med. Biol. **18**, 667–673 (1992).
64. C. H. Schmitz, H. L. Graber, H. Luo, I. Arif, J. Hira, Y. Pei, A. Bluestone, S. Zhong, R. Andronica, I. Soller, N. Ramirez, S.-L. S. Barbour, and R. L. Barbour, "Instrumentation and calibration protocol for imaging dynamic features in dense-scattering media by optical tomography," Appl. Opt. **39**, 6466–6486 (2000).
65. Y. Pei, F.-B. Lin, and R. L. Barbour, "Modeling of sensitivity and resolution to an included object in a homogeneous scattering media and in MRI-derived breast map," Opt. Express **5**, 203–219 (1999).
66. H. L. Graber, Y. Xu, and R. L. Barbour, "Image correction scheme applied to functional diffuse optical tomography scattering images," Appl. Opt. **46**, 1705–1716 (2007).
67. H. Dehghani, M. M. Doyley, B. W. Pogue, S. Jiang, J. Geng, and K. D. Paulsen, "Breast deformation modelling for image reconstruction in near infrared optical tomography," Phys. Med. Biol. **49**, 1131–1145 (2004).
68. H. L. Graber, Y. Pei, R. L. Barbour, D. K. Johnston, Y. Zheng, and J. E. Mayhew, "Signal source separation and localization in the analysis of dynamic near-infrared optical tomographic time series," Proc. SPIE **4955**, 31–51 (2003).
69. J. Mayhew, Y. Zheng, Y. Hou, B. Vuksanovic, J. Berwick, S. Askew, and P. Coffey, "Spectroscopic analysis of changes in remitted illumination: the response to increased neural activity in brain," NeuroImage **10**, 304–326 (1999).
70. A. Corlu, R. Choe, T. Durduran, K. Lee, M. Schweiger, S. R. Arridge, E. M. Hillman, and A. G. Yodh, "Diffuse optical tomography with spectral constraints and wavelength optimization," Appl. Opt. **44**, 2082–2093 (2005).
71. A. Athanasiou, D. Vanel, C. Balleyguier, L. Fournier, M. C. Mathieu, S. Delaloge, and C. Dromain, "Dynamic optical breast imaging: a new technique to visualise breast vessels: comparison with breast MRI and preliminary results," Eur. J. Radiol. **54**, 72–79 (2005).
72. J. Wang, S. Jiang, Z. Li, R. M. diFlorio-Alexander, R. J. Barth, P. A. Kaufman, B. W. Pogue, and K. D. Paulsen, "*In vivo* quantitative imaging of normal and cancerous breast tissue using broadband diffuse optical tomography," Med. Phys. **37**, 3715–3724 (2010).
73. S. Kukreti, A. E. Cerussi, W. Tanamai, D. Hsiang, B. J. Tromberg, and E. Gratton, "Characterization of metabolic differences between benign and malignant tumors: high-spectral-resolution diffuse optical spectroscopy," Radiology **254**, 277–284 (2010).
74. D. R. Busch, W. S. Guo, R. Choe, T. Durduran, M. D. Feldman, C. Mies, M. A. Rosen, M. D. Schnall, B. J. Czerniecki, J. Tchou, A. DeMichele, M. E. Putt, and A. G. Yodh, "Computer aided automatic detection of malignant lesions in diffuse optical mammography," Med. Phys. **37**, 1840–1849 (2010).